



UNSTEADY FLOW PAST ELLIPTIC CYLINDERS

M. T. NAIR AND T. K. SENGUPTA

*Department of Aerospace Engineering, Indian Institute of Technology
Kanpur 208 016, India*

(Received 4 July 1996 and in revised form 28 March 1997)

Flow past elliptic cylinders is investigated for different Reynolds numbers and angles of attack by numerically solving the two-dimensional, unsteady incompressible Navier-Stokes equation. Results are obtained by using various numerical methods for consistency checks and also compared with available experimental results at $Re = 3000$. The Navier-Stokes equation is solved in stream-function-vorticity formulation using a finite difference method with third- and fifth-order upwinding for the convection terms. The pressure field is obtained by solving a Poisson equation and surface pressure values and vorticity information is integrated to obtain the sectional loads and pitching moment. Specific results are provided for $Re = 3000$ and $10\,000$ for different parameter combinations for the early stages of flow development. The effects of Reynolds number, angles of attack (α) and thickness to chord ratios (t/c) are discussed through this two-dimensional direct numerical simulation (DNS).

© 1997 Academic Press Limited

1. INTRODUCTION

THE COMPUTATIONAL methods of unsteady incompressible viscous flow around arbitrary two-dimensional (2-D) bodies have reached a state of maturity where detailed flow analysis is possible. The main aim of the present paper is to analyse the unsteady flow field around elliptic cylinders at large angles of attack which is characterized by massive flow separation, reattachment and pronounced unsteadiness, and to compare it to cases with low angles of attack. For conventional aerofoils with sharp trailing edge at angles of attack well beyond stall, laminar separation occurs near the leading edge, followed by transition in the free shear layer. At high Reynolds number the transition occurs rapidly and the developing turbulent boundary layer is capable of reattaching with the surface quickly—thereby forming a short bubble. For smaller Reynolds numbers and particular angles of attack, the reattachment can occur near the trailing edge without the separated shear layer undergoing transition—forming the so-called long bubble. When the flow is started impulsively from rest, unsteady effects can give rise to high spatial and temporal gradients in the flow. For example, for small angles of attack, separation is seen to occur near the trailing edge at early stages as the flow is established impulsively, and the separation point moves towards the leading edge as time progresses.

The flow field around elliptic cylinders shares some common characteristics with that for streamlined bodies like aerofoils and bluff bodies like circular cylinders. A very comprehensive review of flow past circular cylinders is provided by Williamson (1996). He classifies the various vortex shedding regimes found experimentally and computationally, depending on the Reynolds number. Accordingly, the present set of computations belong to the *Shear-Layer Transition Regime*. The name derives from the fact that the flow dynamics is determined by the transition of the detached shear layer, following flow separation on the body. Williamson (1996) states that “the Kelvin-Helmholtz instability of the shear layers is principally two dimensional as for a shear

layer... and contributes to the rise of 2-D Reynolds stresses and thereby the rise in base suction." This idea that the 2-D equations can be studied to understand the formation and shedding of vortices in the Reynolds number range between 1 000 and 200 000 has been used in Braza *et al.* (1986) and Sengupta & Sengupta (1992, 1994) for circular cylinders. Nair & Sengupta (1996) have also investigated the flow field around circular and elliptic cylinders at zero angle of attack to study the onset of asymmetry in the near wake at high Reynolds numbers. The present investigation extends the previous study by considering flow past elliptic cylinders of different thickness-to-chord ratios at different angles of attack by solving the 2-D Navier-Stokes equation.

Lugt & Haussling (1974) have studied numerically the laminar incompressible flow past ellipses. They computed the flow past elliptic cylinders of various t/c ratios for Reynolds numbers of 15, 30 and 200 at an angle of attack of 45° . Mehta & Lavan (1975) have studied flow past a 9% thick Joukowski aerofoil for $Re = 1\,000$ and an angle of attack of 15° . They have used a grid generated by conformal mapping—which altered the aerofoil shape near its trailing edge significantly. They discussed in detail the phenomenon of a starting vortex, bubble formation and stall. Ohmi *et al.* (1990, 1991) have done both an experimental and a computational study of the flow field around oscillating and translating elliptic cylinders and aerofoils for $Re = 3\,000$ started impulsively. Deng *et al.* (1994) have studied numerically the flow field around NACA 0012 aerofoils for early times at $Re = 1\,000$ and $10\,000$. Morikawa & Gronig (1995) have given experimental and computational results for translating and oscillating NACA 0015 aerofoils at $Re = 35\,000$ for an accelerated start. Further experimental results for flow past elliptic cylinders can be obtained in Modi & Dikshit (1975) and Shintani *et al.* (1983) for subcritical flows. Ota *et al.* (1975) and Krishnamurthy (1992) have provided detailed surface pressure data for elliptic cylinders in the critical Reynolds number range.

The flow around elliptic and conventional aerofoils at high angles of attack at moderate Reynolds number is usually dominated by the following main events:

- (i) the instability of the unsteady flow in general and the Kelvin-Helmholtz instability of the instantaneous detached shear layer in particular;
- (ii) the bubble formation over the body and their movements—which determines the loads and moment experienced by the body;
- (iii) the vortex interactions in the wake;
- (iv) the *alleyway* formation, which is a consequence of the above three; this is essentially an unsteady effect due to which the flow accelerates over the lower surface and the streamlines below the lower surface wrap around the vortices over the top surface and detach them.

The Kelvin-Helmholtz instability dominates bluff body flows—as has been explained by Williamson (1996) and shown numerically by Nair & Sengupta (1996) for the case of circular and elliptic cylinders at zero angle of attack in describing the onset of asymmetry. In this paper we study all the above events for elliptic cylinders at different angles of attack and Reynolds numbers.

Here the Navier-Stokes equation is solved by a finite difference method using higher-order upwinding for the convective terms. Upwind schemes are preferred for reasons of high accuracy of the results and numerical stability at high Reynolds numbers. The upwinding suppresses any non-physical oscillations that would be present otherwise. At the same time one would not like to alter the physical dissipation, and this can be achieved by resorting to higher-order upwinding. For convection-dominated flows at high Reynolds numbers the smaller scales become important, and any numerical scheme should therefore avoid introducing spurious dispersion at high wave

numbers. In numerical computations, the sub-grid scale kinetic energy is smaller than the sub-grid scale diffusion and thus a second-order accurate scheme appears to be sufficient, as such results exhibit the correct kinetic energy distribution [see Schumann (1987)]. However, for large Reynolds number flows it is important to describe the mean advection problem accurately. For these practical situations, pseudo-spectral or higher-order schemes are necessary. These higher-order methods are finding more and more applications in direct and large eddy simulations; see, for example Rai & Moin (1991) and Najjar & Vanka (1995). The various aspects of phase and dissipation errors of various schemes have been described in Sengupta & Sengupta (1994). In the present investigation, apart from using the third-order upwinding scheme, a fifth-order method has been used for the convective terms of the vorticity transport equation. The third-order scheme is a modification of the scheme proposed by Kawamura *et al.* (1985). This scheme has also been used in Nair & Sengupta (1996) to investigate the onset of asymmetry for flow past circular and elliptic cylinders at zero angles of attack.

For 2-D flows it is advantageous to work with fewer unknowns, as in stream function and vorticity formulations. However, the loads and moment on the body cannot be obtained accurately and directly from the stream function and vorticity values in the flow field. For this purpose one would require to solve a Poisson equation for pressure. Pressure solutions are obtained here at any instant of time from the stored stream function values in the whole field.

Here the incompressible flow past impulsively started elliptic cylinders of t/c ratio of 0.1 and 0.25 is computed for Reynolds number of 3000 and 10 000 without making any effort to model turbulence. It is expected that both the upwind schemes used here will provide a 2-D direct numerical simulation. The set of results for $Re = 3000$ and $t/c = 0.1$ at 30° angle of attack has been compared with experimental results of Ohmi *et al.* (1990). Detailed pressure solutions giving pressure contours and the surface pressure are also presented, along with the integrated lift, drag and pitching moment.

2. FORMULATION

The unsteady Navier-Stokes equation for incompressible 2-D flows are solved here in a stream function and vorticity formulation and are given by

$$\nabla^2 \psi = -\omega, \quad (1)$$

$$\frac{\partial \omega}{\partial t} + \nabla \cdot (\omega \mathbf{V}) = \frac{1}{Re} \nabla^2 \omega. \quad (2)$$

All lengths are nondimensionalized with respect to the chord of the elliptic cylinder and the velocities by the free-stream value. The nondimensional time is defined with reference to a time scale constructed directly from the velocity and length scale.

Equations (1) and (2) are solved in an orthogonal transformed plane (shown in Figure 1), where the equations are represented as

$$\frac{\partial}{\partial \xi} \left(\frac{h_2}{h_1} \frac{\partial \psi}{\partial \xi} \right) + \frac{\partial}{\partial \eta} \left(\frac{h_1}{h_2} \frac{\partial \psi}{\partial \eta} \right) = -h_1 h_2 \omega, \quad (3)$$

$$h_1 h_2 \frac{\partial \omega}{\partial t} + h_2 u \frac{\partial \omega}{\partial \xi} + h_1 v \frac{\partial \omega}{\partial \eta} = \frac{1}{Re} \left\{ \frac{\partial}{\partial \xi} \left(\frac{h_2}{h_1} \frac{\partial \omega}{\partial \xi} \right) + \frac{\partial}{\partial \eta} \left(\frac{h_1}{h_2} \frac{\partial \omega}{\partial \eta} \right) \right\}, \quad (4)$$

in which h_1 and h_2 are the scale factors of the transformation as described in Sengupta & Sengupta (1994). The components of velocity in transformed plane are given by

$$u = \frac{1}{h_2} \frac{\partial \psi}{\partial \eta}, \quad v = -\frac{1}{h_1} \frac{\partial \psi}{\partial \xi}. \quad (5)$$

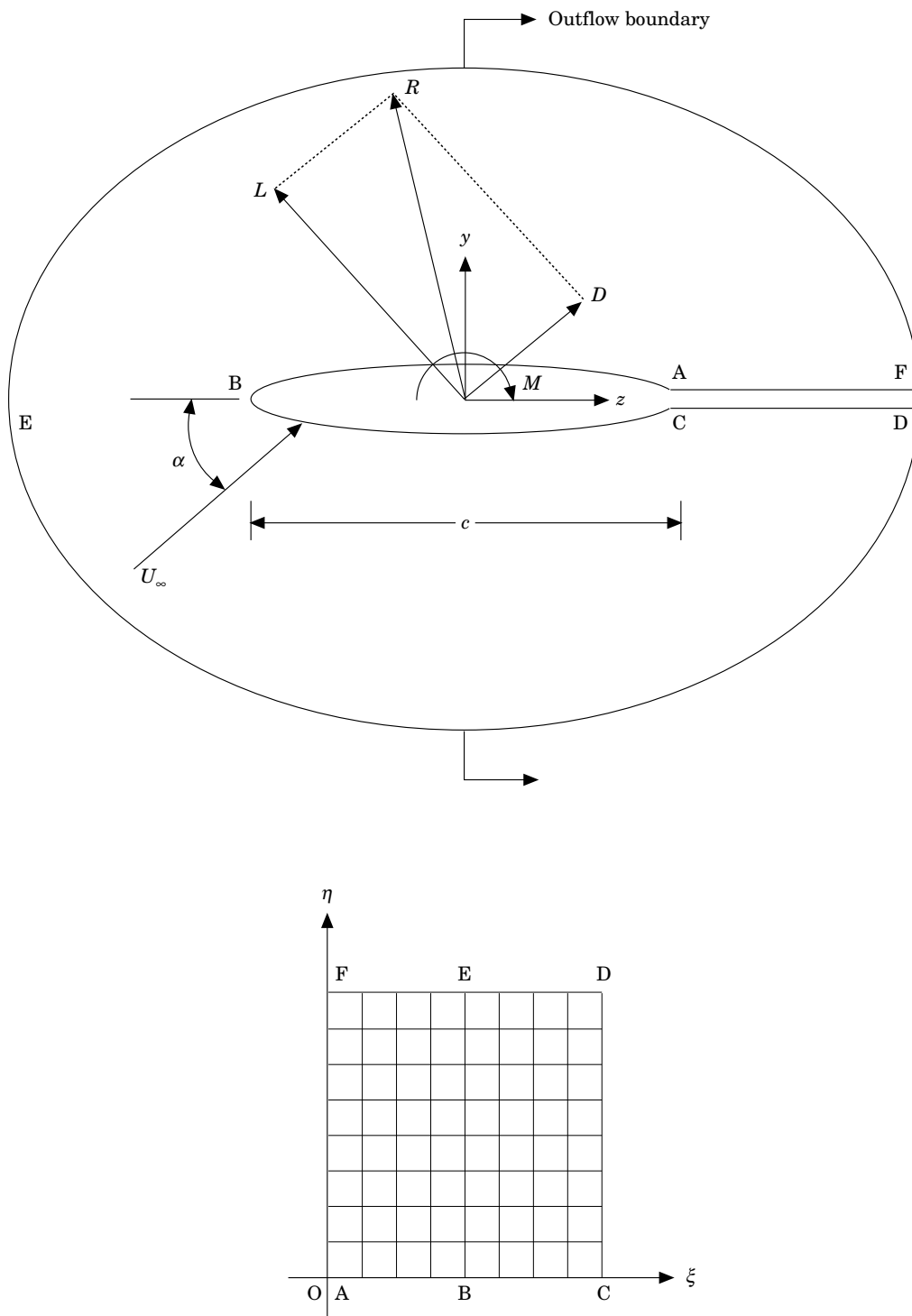


Figure 1. The physical and computational domain. α = angle of attack; c = chord; L = lift; D = drag; R = resultant; M = pitching moment; U_∞ = freestream velocity.

The analytical orthogonal transformation used for the elliptic aerofoil is given by

$$x = a \cos 2\pi\xi \cosh[(\eta_2 - \eta_1)\eta + \eta_1], \quad y = a \sin 2\pi\xi \sinh[(\eta_2 - \eta_1)\eta + \eta_1], \quad (6)$$

where a is the focal distance and $\eta = \eta_1$ is the ellipse and $\eta = \eta_2$ represents the outer boundary in the transformed plane.

The governing Poisson equation for pressure is obtained by taking the divergence of the Navier-Stokes equation in primitive variables. For an orthogonal curvilinear coordinate system this is given by

$$\nabla^2 p = \frac{\partial(v\omega)}{\partial x} - \frac{\partial(u\omega)}{\partial y}. \quad (7)$$

In the orthogonal transformed plane, equation (7) is given by

$$\frac{\partial}{\partial\xi} \left(\frac{h_2}{h_1} \frac{\partial p}{\partial\xi} \right) + \frac{\partial}{\partial\eta} \left(\frac{h_1}{h_2} \frac{\partial p}{\partial\eta} \right) = \frac{\partial}{\partial\xi} (h_2 v \omega) - \frac{\partial}{\partial\eta} (h_1 u \omega). \quad (8)$$

3. INITIAL AND BOUNDARY CONDITIONS

On the solid surface of the boundary ABC (in Figure 1) the no-slip conditions are applied

$$\psi = \text{constant}, \quad \frac{\partial\psi}{\partial\eta} = 0. \quad (9)$$

These conditions fix the wall vorticity, which is the required boundary condition for the vorticity transport equation. Periodic boundary conditions apply at AF and CD for all variables. For the stream function equation at the outer boundary, the velocity boundary condition (Neumann condition) is used. For equation (4) at the outflow boundary, the diffusion operator is switched off; i.e., locally, an Euler equation is solved. For the rest of the outer boundary, the following condition is used:

$$\frac{\partial\omega}{\partial\eta} = 0. \quad (10)$$

For the pressure Poisson equation, equation (8), a Neumann boundary condition, as obtained from the momentum equations, is used on the boundaries.

Inviscid irrotational flow is taken as the initial solution and is obtained by solving equation (3) with $\omega = 0$.

4. NUMERICAL METHOD

For the solution of Poisson equations (3) and (8), the alternating direction implicit (ADI) method of Peaceman & Rachford, as given in Ames (1992), and the modified strongly implicit procedure (MSIP) of Schneider & Zedan (1981) are used. In general, the equations are discretized at the cell nodes, while the pressure equation is discretized at the cell centres at the boundaries. This latter procedure is similar to that described in Abdallah (1987).

For the vorticity transport equation, the diffusion terms are discretized using second-order central differencing. The convection terms are discretized by higher-order upwinding. As has been shown in Sengupta & Sengupta (1994), all discretizations act like a low pass filter, giving rise to significant phase error at high wave numbers—with the cut-off defined by the Nyquist criterion. Additionally, the high Reynolds number

flows require artificial dissipation to avoid numerical instability. The higher-order upwind schemes not only minimize the phase error but also add lesser numerical dissipation (refer to Figure 2). It should be pointed out that, because of the nonlinear nature of the filter, an increase in spatial resolution brings about larger improvements of these schemes. In this context the effects of an *inverse error cascade* and the principle of uncertainty have to be borne in mind for all large eddy simulation (LES) and direct numerical simulations (DNS)—which is discussed in Lesieur & Métais (1996).

Here two upwind schemes have been used, the first method being a variant of the scheme proposed by Kawamura *et al.* (1985). For the third-order upwind scheme of Kawamura *et al.* (1985), the convection terms are discretized as

$$u \frac{\partial \omega}{\partial x} = u \frac{\partial \omega}{\partial x} \Big|_{\text{CD4}} + 3 |u| \frac{\Delta x^3}{4!} \frac{\partial^4 \omega}{\partial x^4}. \quad (11)$$

The left-hand side is the finite difference representation of the convection terms and in this scheme the right-hand side is an implicit blend of a fourth-order central difference operator (as represented by the first term) and a numerical dissipation term represented by the last term. For many high Reynolds number flow calculations we have found that the numerical dissipation as given by equation (11) is excessive [in the scheme of Kawamura *et al.* (1985) this is three times the leading truncation error term]. In our modified third-order method we explicitly control this numerical dissipation. For the fifth-order upwind scheme, as used in Rai & Moin (1991) and Najjar & Vanka (1995), the convection terms are written as

$$u \frac{\partial \omega}{\partial x} = u \frac{\partial \omega}{\partial x} \Big|_{\text{CD6}} + |u| \frac{\Delta x^5}{6!} \frac{\partial^6 \omega}{\partial x^6} \quad (12)$$

The resolution of the fifth-order scheme is compared with other central and upwind schemes in Figure 2. In this figure the fifth-order scheme corresponds to equation (12); the third-order scheme is due to Kawamura *et al.* (1985) and the QUICK scheme is due to Leonard (1978) (a third order upwind method). Figure 2(a) shows the equivalent real part of the spectral representation of the schemes and Figure 2(b) gives the numerical dissipation.

One can estimate the truncation errors of both these methods. The truncation error of the fifth-order method is indistinguishable from the machine round-off error (in double precision) for the grid used in these computations. The corresponding truncation error of the third-order scheme is seven orders of magnitude larger. Also the fifth-order upwind method will be far more effective in controlling errors at high wave numbers, as the truncation error is proportional to the sixth derivative of the variable, as shown in Figure 2(a).

5. RESULTS AND DISCUSSION

For all the computations reported here, an analytically generated O-type grid is used. There are 201 points on the surface of the ellipse, and either 201 or 301 points are taken in the normal direction such that outer boundary remains at the same distance for both t/c (thickness-to-chord) ratio cases. For physical reasons a nondimensional time step of 0.001 or 0.0001 was chosen, depending on the nature and extent of the separated flow over the ellipse. For the higher angle of attack ($\alpha = 30^\circ$) case, the strong separation excites higher frequencies in the recirculating region requiring smaller time steps. Detailed comparisons of results for elliptic cylinders are made in Nair &

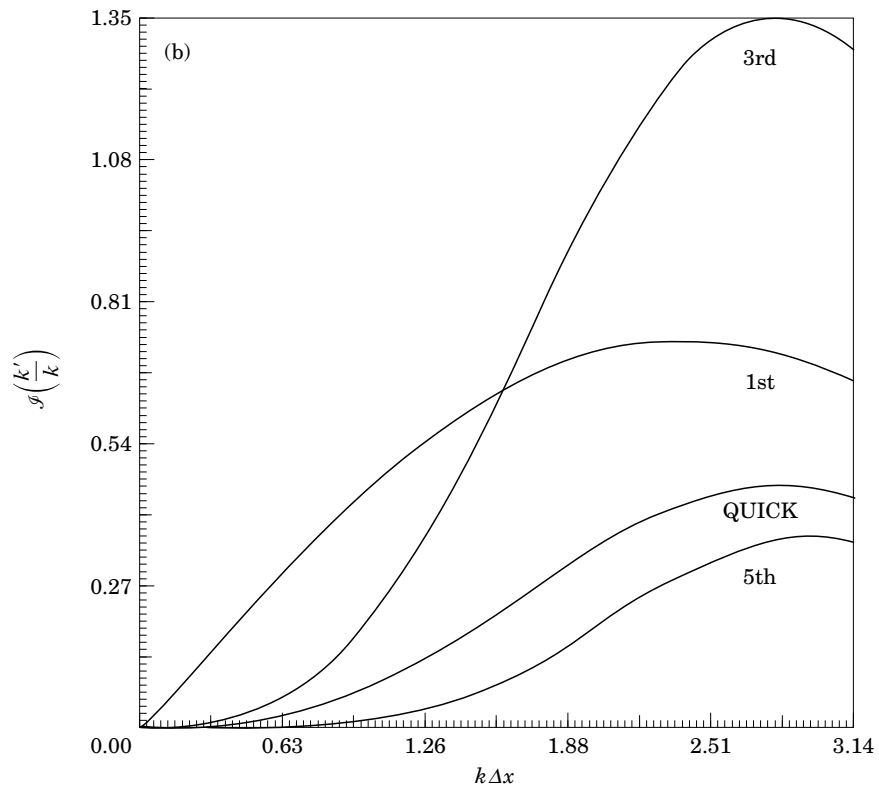
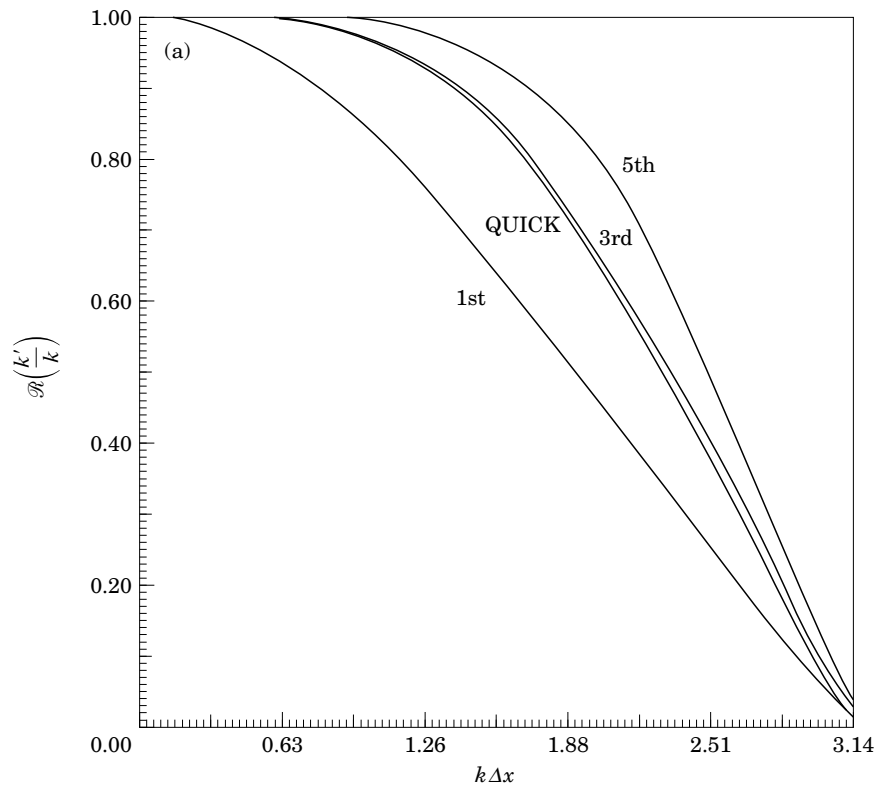


Figure 2. Spectral representation of different upwind schemes. The order of upwinding is as indicated in the figures. (a) Phase representation; (b) numerical dissipation.

Sengupta (1996) for the zero angles of attack cases at $Re = 10\,000$ for two t/c ratios with the circular cylinder case. Here two Reynolds numbers (3 000 and 10 000) and two t/c ratio (0.1 & 0.25) combinations along with three angles of attack cases ($\alpha = 10^\circ, 12^\circ$ & 30°) are investigated. While some comparisons are shown using the third-order upwind scheme, most of the computations are performed using the fifth-order upwind scheme. Unless otherwise specifically stated, the results are obtained using fifth-order upwinding. Both the ADI and MSIP methods have been used for solving the Poisson equations [equations (3) and (8)]. The results obtained are indistinguishable and hence not reported separately. The accuracy of the present method is well established in the results presented in Sengupta & Sengupta (1992, 1994) for circular cylinders at high Reynolds numbers, and in Nair & Sengupta (1995, 1996) for elliptic cylinders at zero angle of attack. In all this work, the ADI method was used for solving the stream function equation. Pressure results are presented here for the first time. It is noted that, after the impulsive start, the ADI method performs better, while MSIP performs better subsequently. Also, MSIP allows taking larger time steps compared to the ADI method. For the convergence check of the solution for stream function and pressure we have used a tolerance of 10^{-5} for solution residue at every point in the flow field.

5.1. CASE 1: $Re = 3\,000$, $t/c = 0.1$ AND $\alpha = 30^\circ$

The computed results for this case are first compared with the experimental visualization pictures of Ohmi *et al.* (1990). The comparison in Figure 3 shows the ability of the present method to reproduce the flow details. The evolution of the flow from impulsive start is shown in Figure 4(a) through the stream function contour plots. The corresponding vorticity contours are shown in Figure 4(b). In Figure 3 there are two sets of computational results; one corresponding to the third-order and the other to fifth-order upwind scheme of solving the vorticity transport equation. It is to be noted that, even for smaller times, there are significant differences in the near field. The flow visualization pictures do not reveal these, and hence do not permit us to compare the computational methods in detail. Nonetheless, the overall features, namely the location and size of the recirculation zones, are predicted to a fair degree by both the schemes.

For this case at $t = 1.0$, apart from the three vortices near the leading edge, one can locate a bubble near the trailing edge on the top surface. The surface pressure distributions are shown in Figure 4(c). The lift, drag and pitching moment coefficient about the leading edge are shown in Figure 8 for all the $Re = 3000$ cases; these are calculated at the discrete times shown in the figure. The initial increase in lift prevails till $t = 2$,[†] when the rearmost of the leading edge vortices is about to be detached. The rotation and the proximity of the vortex causes the lift to achieve a maximum. However, the flow is very unstable at this instant due to the presence of a nonorthogonal saddle point. This can be ascertained from Figure 5, where we have plotted the ξ -component of the velocity at the three stations, as marked in the figure. This result is in conformity with similar results presented in Nair & Sengupta (1995). Such temporal instabilities are also seen at $t = 6.5, 15$ and 19 . Following this, the primary vortex detaches from the surface and the surface pressure peak continues its rearward movement while the pressure magnitude comes down. This also leads to higher drag, and the pitching moment displays stable nose down attitude.

From $t = 2.5$ onwards one can also notice the formation of an *alleyway* where the streamlines from the lower surface turn around the trailing edge bubble. This alters

[†] The time t here and hereafter should not be confused with t , the thickness, as in t/c .

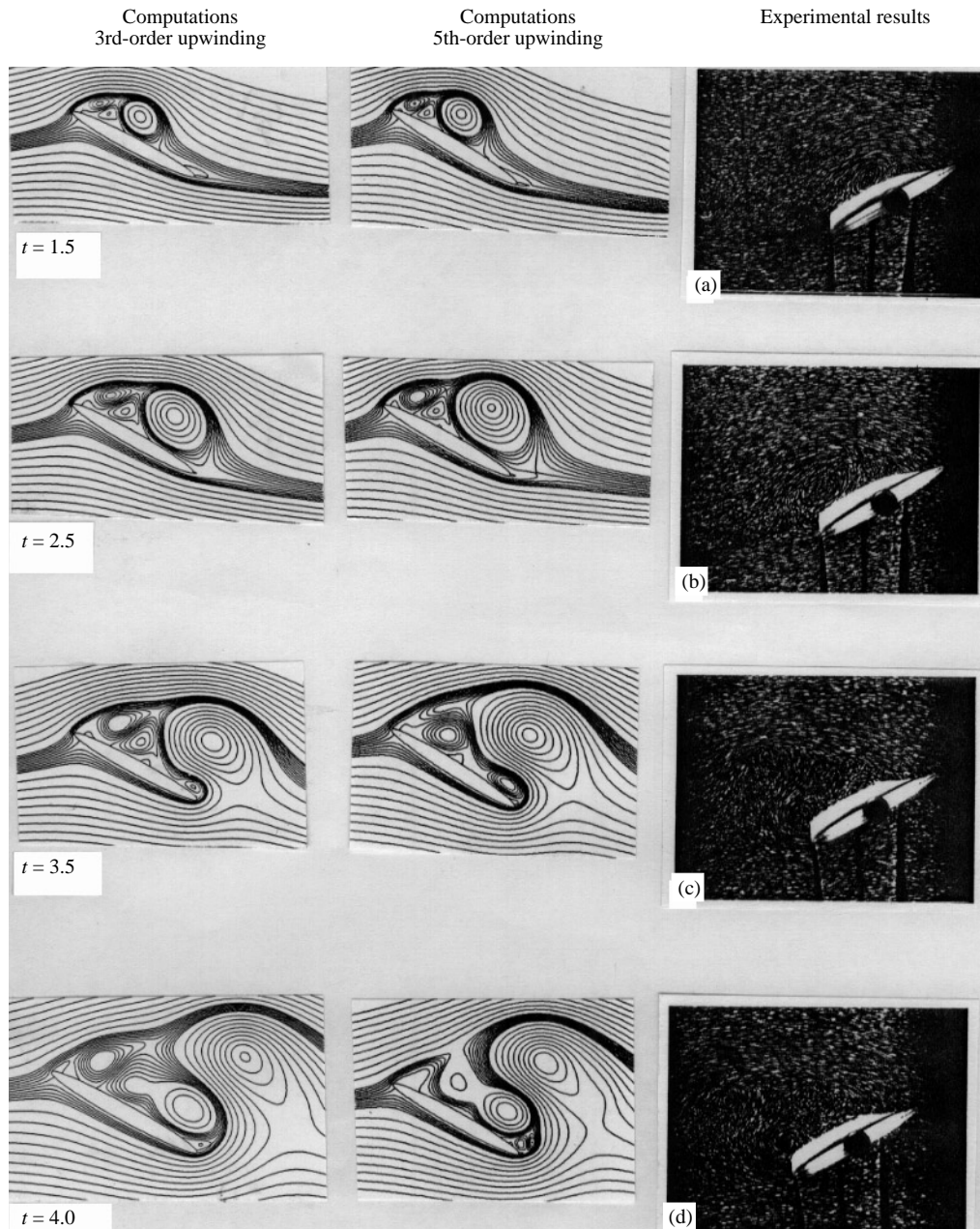


Figure 3. Comparison between the present computation and experiments by Ohmi *et al.* (1990) for $t/c = 0.1$, $Re = 3000$ and $\alpha = 30^\circ$.

the streamline curvature over the lower surface, which in turn causes a suction over the lower surface. This is the reason for such a rapid loss of lift from $t = 2.0$ to $t = 3.5$. Perry *et al.* (1982) have provided some descriptive understanding of near-wake vortex formation, and they have used the terminology 'alleyway' to describe the vortex shedding phenomena by examining instantaneous streamlines. At $t = 3.5$ the presence of a large recirculation region near the trailing edge causes the suction peak to strengthen, but the corresponding low pressure on the lower surface gives rise to

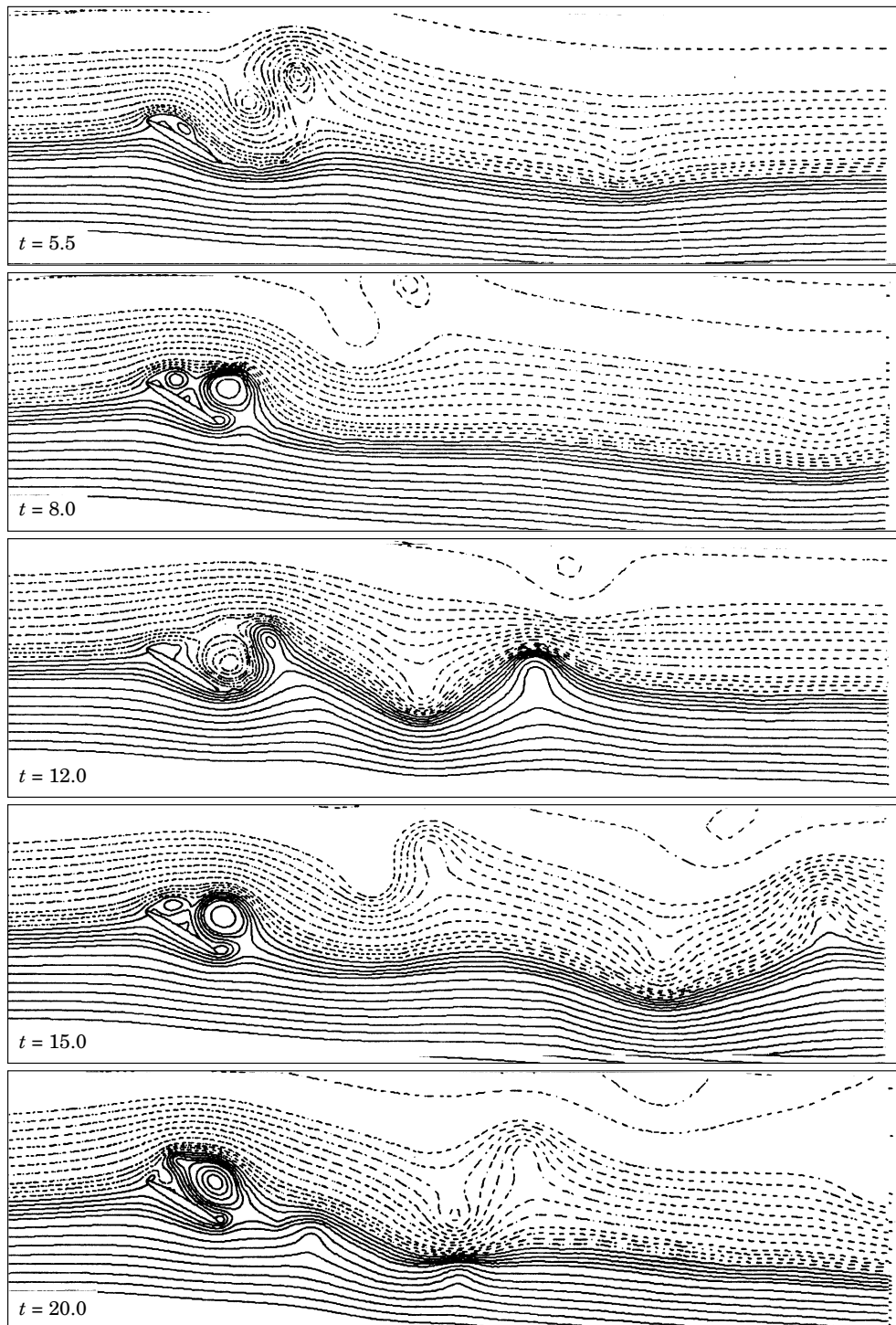


Figure 4(a). Streamline contours for an elliptic cylinder of $t/c = 0.1$, $Re = 3000$ and $\alpha = 30^\circ$ at times indicated in the figures.

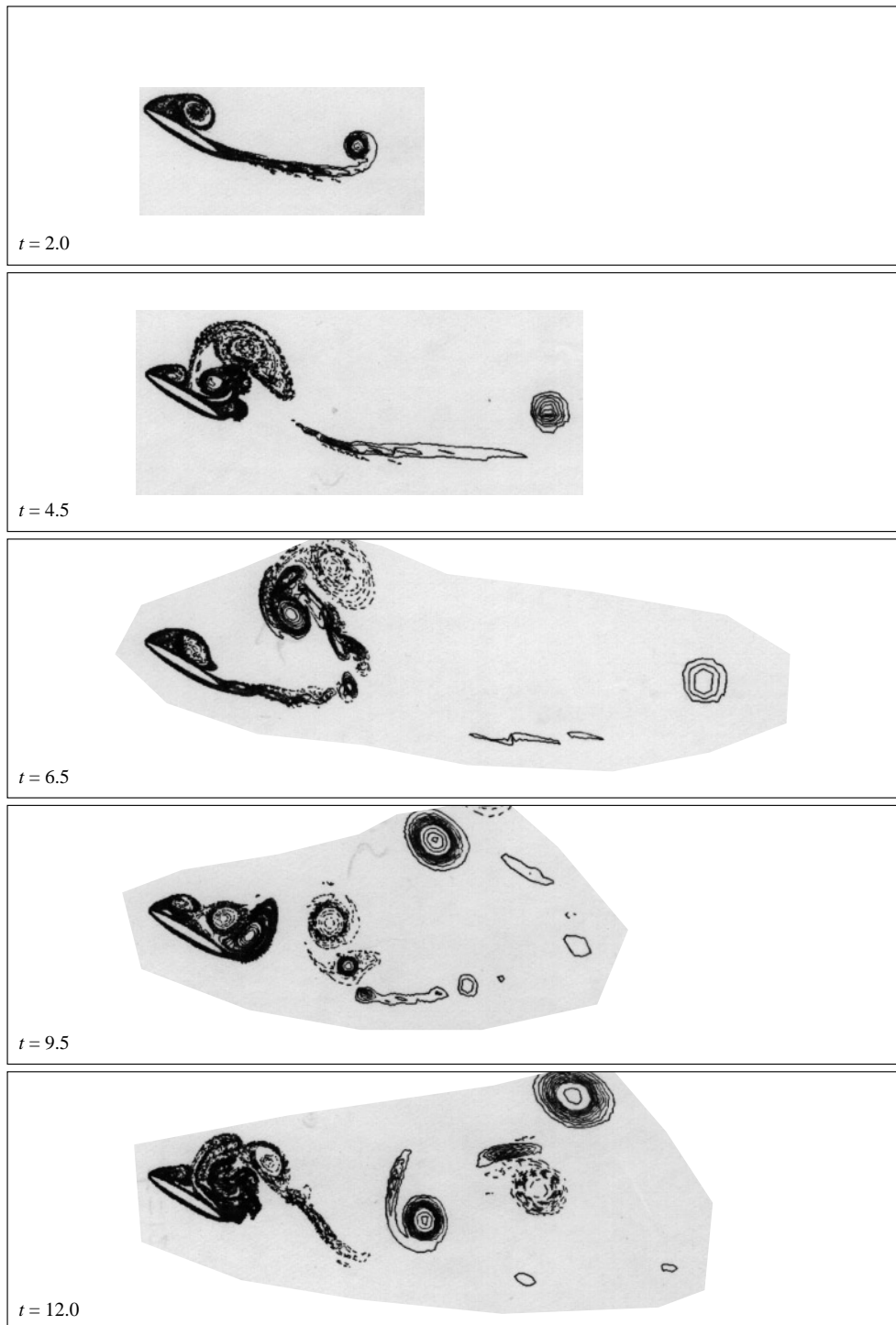


Figure 4(b). Vorticity contours for an elliptic cylinder of $t/c = 0.1$, $Re = 3000$ and $\alpha = 30^\circ$ at times indicated in the figures.

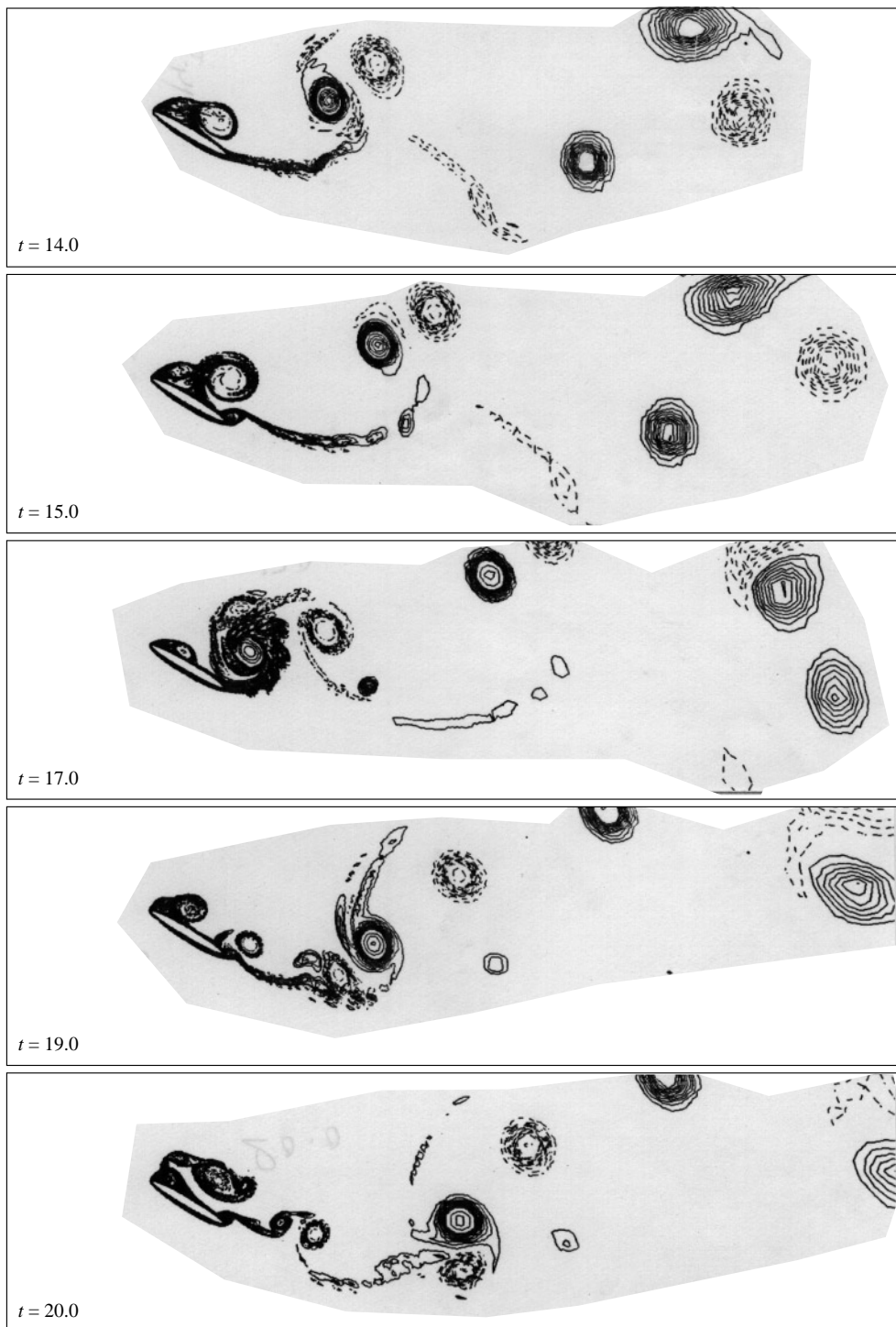


Figure 4(b). (Continued.)

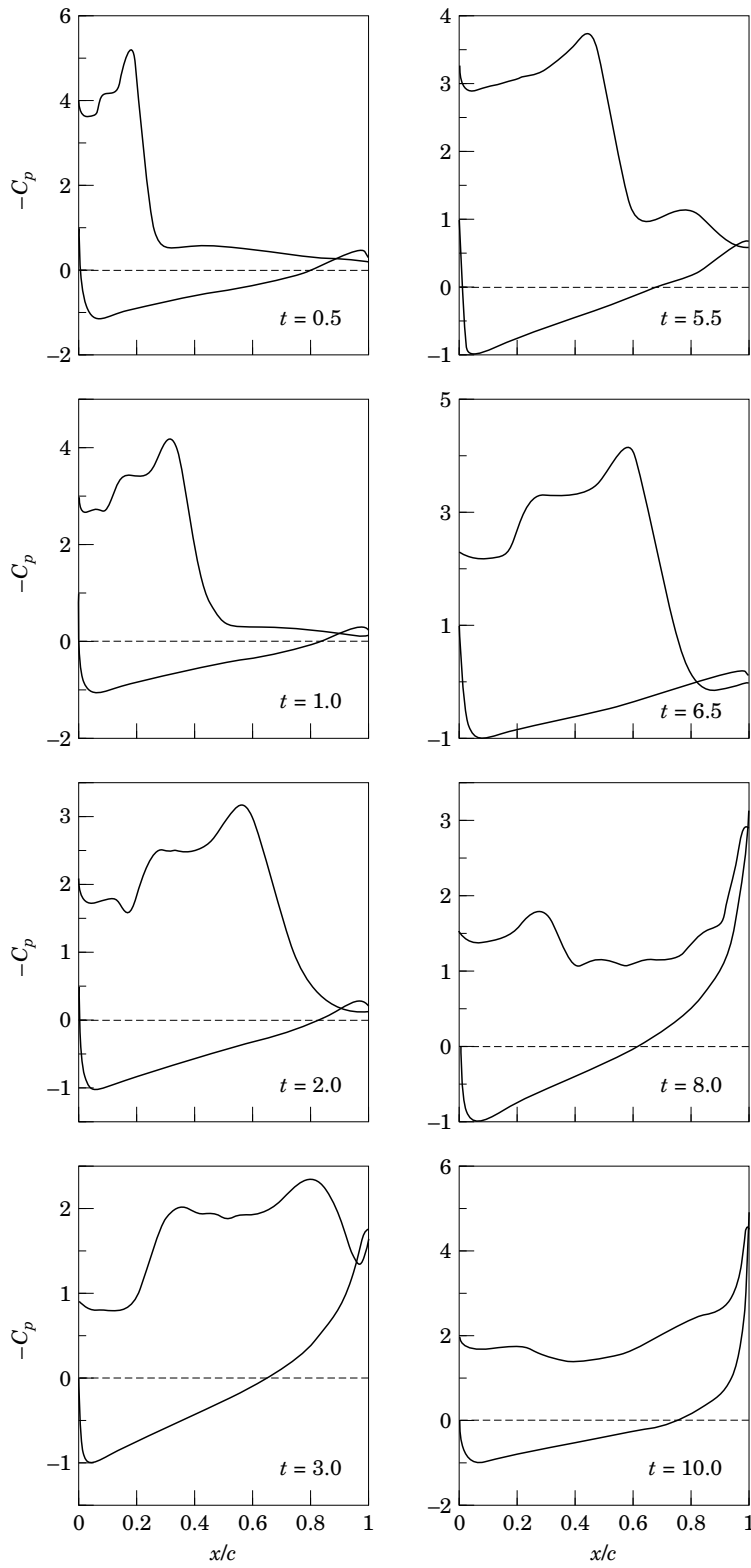


Figure 4(c) C_p distribution for the case of $t/c = 0.1$; $Re = 3000$ and $\alpha = 30^\circ$.

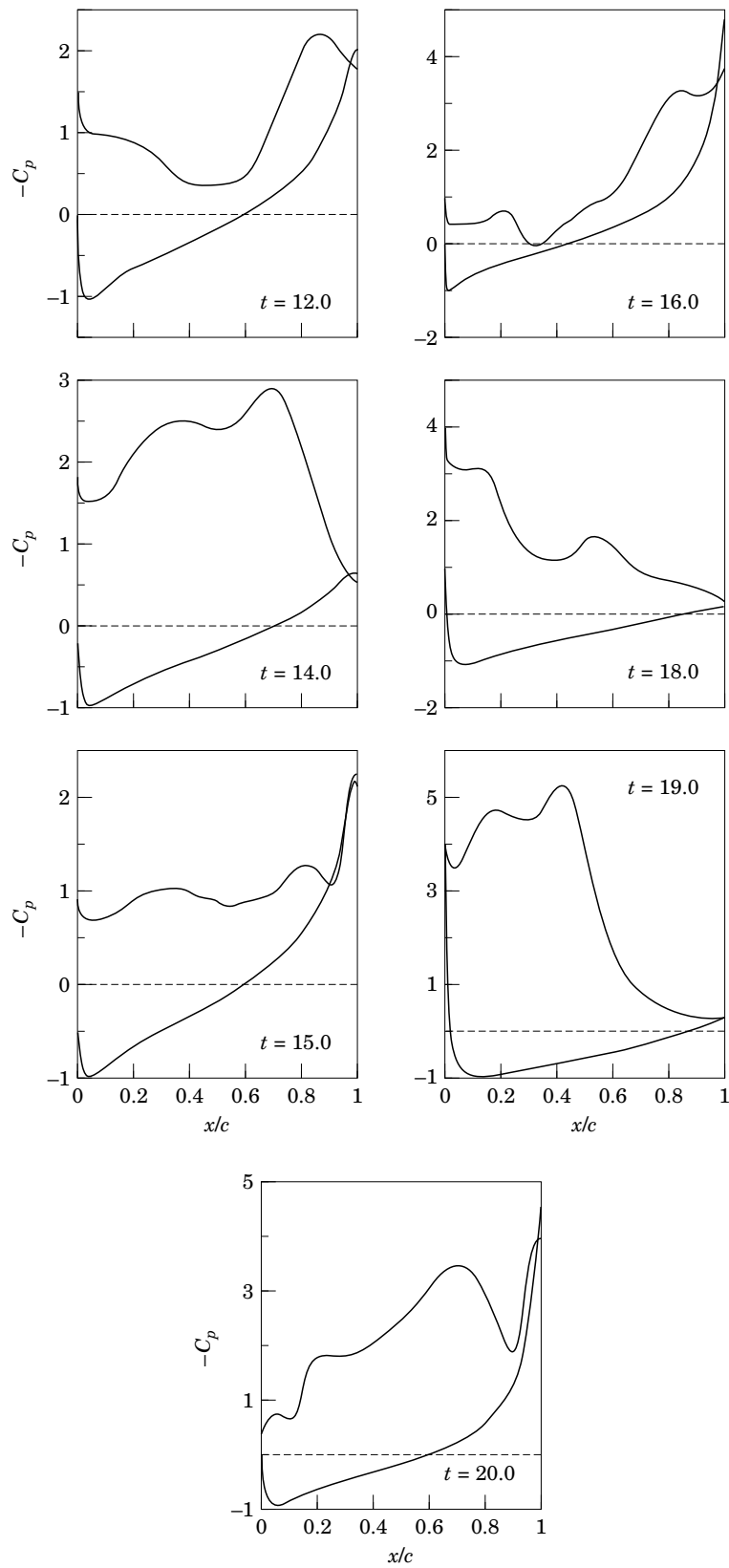


Figure 4(c). (Continued.)

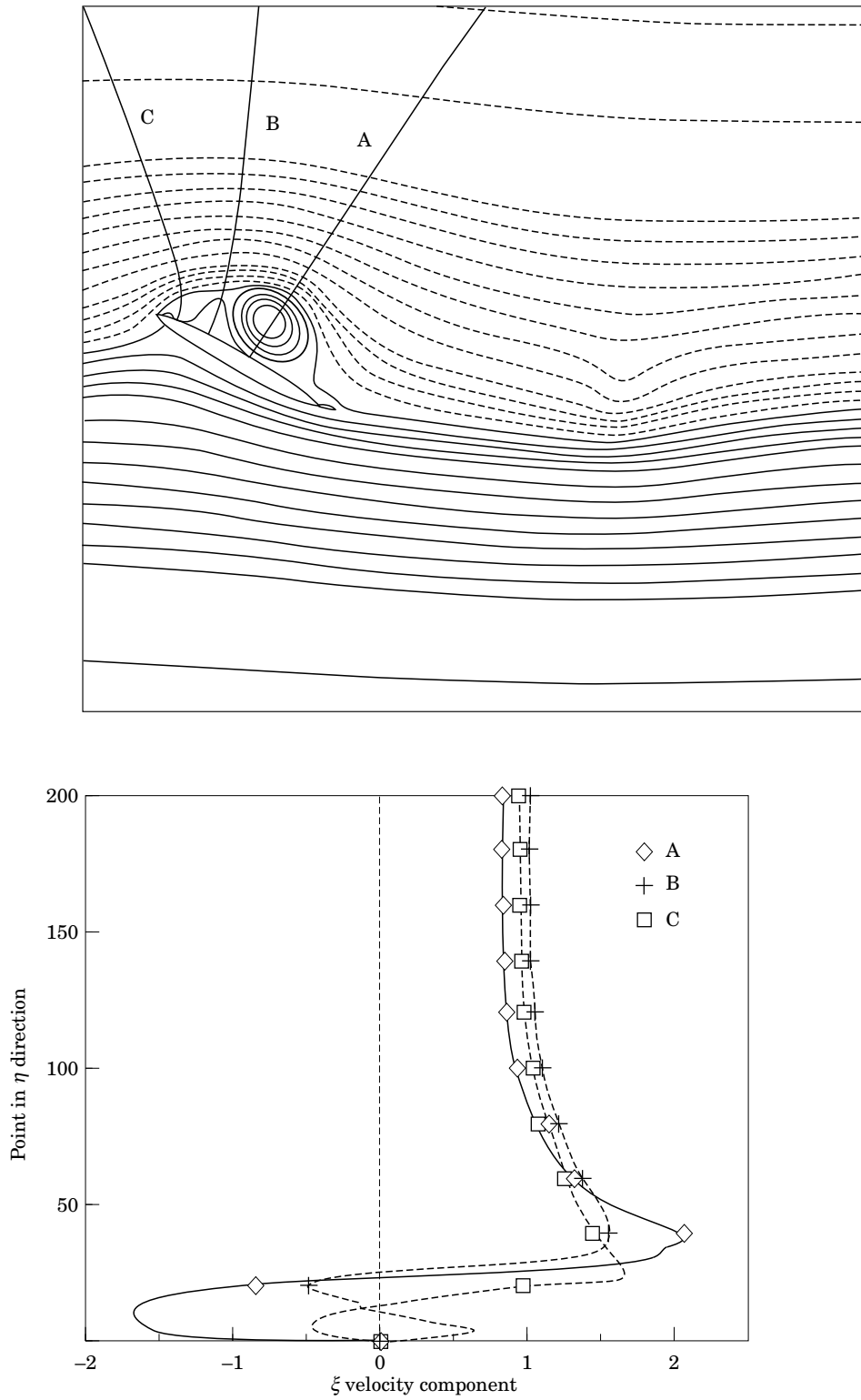


Figure 5. ξ component of velocity profiles at the three different stations at $t = 2$.

minimum lift and maximum drag. At this instant one can notice another large bubble near the leading edge which detaches from the surface and migrates towards the trailing edge, causing a drop in the suction pressure. From $t = 4.5$ to $t = 5.5$ we see the evolution of the leading edge bubble, and at $t = 5.5$ the bubble is over the whole length of the top surface; this once again loads the ellipse in the fore portion, reducing drag and pitching moment very rapidly. After this the bubble starts reducing in size, and at $t = 6.5$ the flow is similar to the flow at $t = 2.0$ —once again, the presence of a saddle point indicating strong flow instability followed by break-up of the bubble. The surface pressures look similar, but the top surface suction peak value is much higher and at the same time the lower surface pressure values are smaller. This gives rise to the maximum of lift at $t = 6.5$. The lift thereafter continues to decrease till $t = 8.0$, in the same sequence as we have seen between $t = 2.0$ and $t = 3.5$. Beyond $t = 8.0$ a completely new sequence of events unfolds. At this time a saddle point can be spotted over the mid-chord location of the ellipse which causes flow instability locally, thereby forming an alleyway which accelerates the flow over lower surface, causing the lift to drop. Subsequent increase of lift is due to the formation of a bubble near the trailing edge, which grows in size and in the process removes the alleyway; hence, there is a pressure recovery on the lower surface. Thus, while the bubble formation leads to increase in lift, the loss of lift could be attributed to the appearance of an alleyway. The latter can be traced at $t = 3.0, 8.0, 10.0, 15.0, 16.0$ and 20.0 from the streamline contours and C_p distributions.

Similarly, the Kelvin-Helmholtz instability of the free shear layer can be detected at $t = 5.5, 6.5, 12.0$ and 13.0 from both the streamline and vorticity contours. In the streamline contours these appear as wavy streamlines and in vorticity contours as chains of small vortices.

There is a curved cluster of vortices convecting together in the wake originating at $t = 9.5$. There are two strong vortices with weaker vortices linking them. As they convect downstream, the linking vortices slowly diffuse, leaving only three vortices. These three vortices interact with one another; two of them coalesce and the resulting pair convects downstream. Also notice the strong negative vortex shed at $t = 4.5$ which stays closer with the positive vortex of the above-mentioned cluster and at $t = 15.0$ migrates downstream to interact with the positive vortex. This interaction leads to severe distortion of the negative vortex and eventual tearing, as can be seen in Figure 4(b) from $t = 17.0$ onwards. The swing of the entire wake can be seen in Figure 4(a) up to $t = 20.0$. The large increase in lift could be attributed to the formation of the leading edge bubble starting at $t = 17.5$ up to $t = 19.0$ and subsequent drop due to bursting of the bubble. The transverse extent of the bubble also gives rise to the largest drag, experienced at $t = 19.0$. Similar vortex interaction results are given in Najjar & Vanka (1995) for a normal flat plate in a uniform stream at a Reynolds number of 500.

5.2. CASE 2: $Re = 3000$, $t/c = 0.1$ AND $\alpha = 10^\circ$

The early stages of flow evolution for this case is characterized by slow growth of longer bubble. The vorticity contours are shown in Figure 6(a) and the C_p distribution in Figure 6(b). The loads and moment are shown in Figure 8. At $t = 2.0$ a narrow bubble forms near the leading edge which increases in length and strength, and eventually the reattachment point merges with the rear stagnation point at $t = 4.0$. At the same time another bubble forms under the separating streamline. This effectively increases the thickness of the body which shows up in growth of lift. The slow increase in lift in this case is due to the increase in suction pressure on the rear half of the

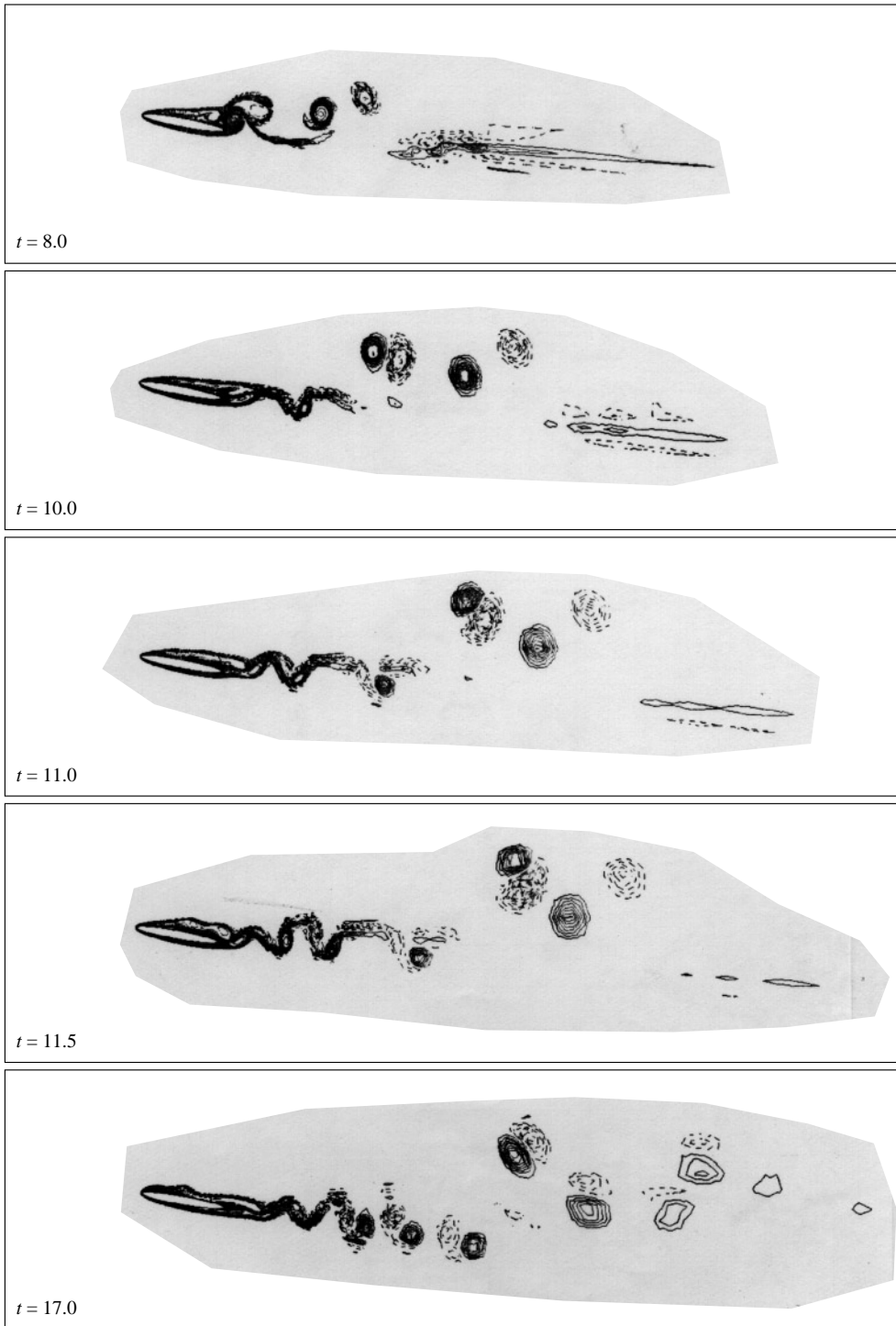


Figure 6(a). Vorticity contours for the case of $t/c = 0.1$, $Re = 3000$ and $\alpha = 10^\circ$ at times indicated in the figures.

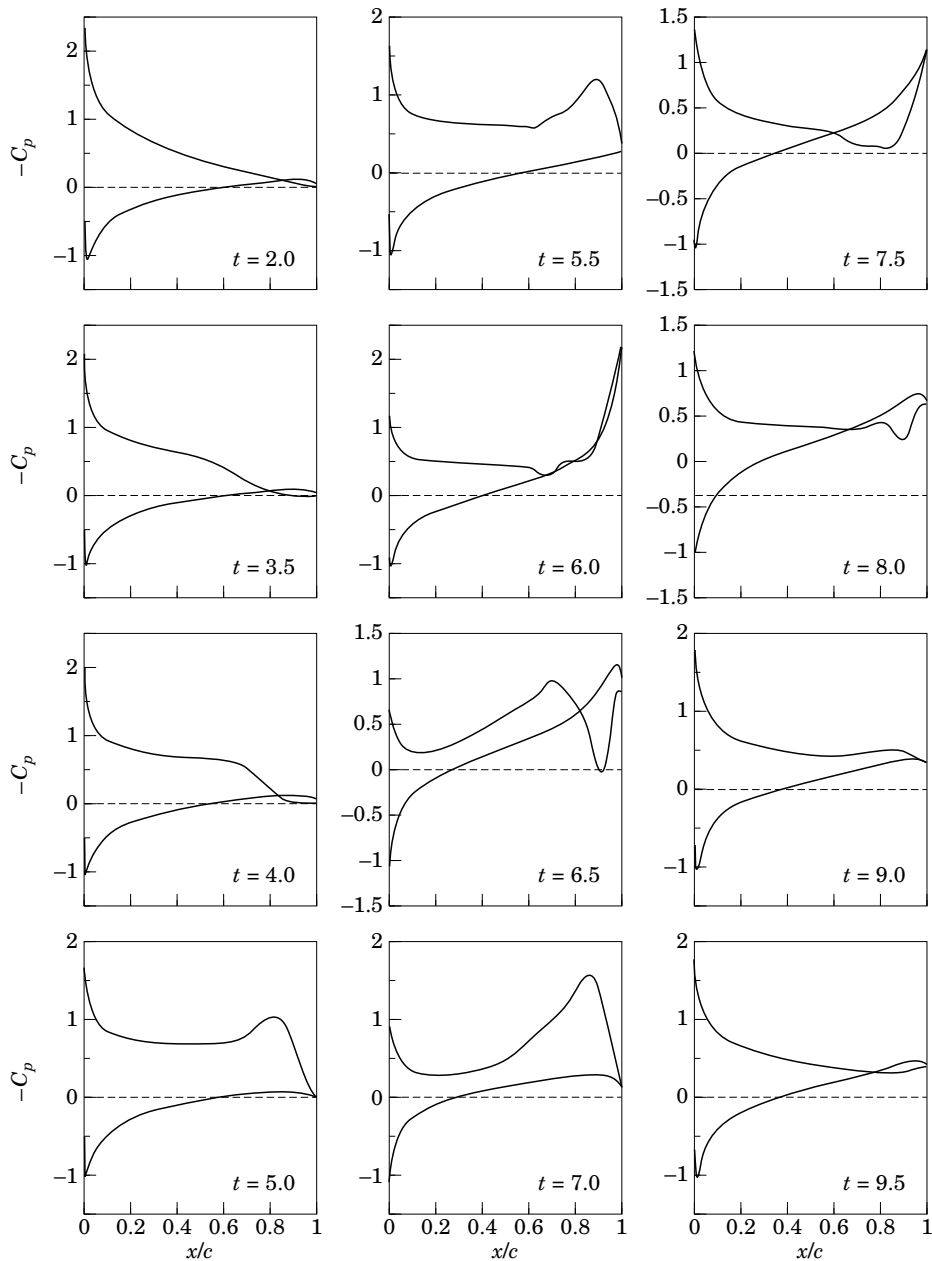


Figure 6(b). C_p distribution for the case of $t/c = 0.1$, $Re = 3000$ and $\alpha = 10^\circ$.

aerofoil which increases the pitching moment up to $t = 5.0$. The long bubble bursts at $t = 5.0$, despite which the lift continues to increase till $t = 5.5$ because of the induced effect of a smaller bubble forming near the trailing edge. At $t = 6.0$ we notice the loss of lift over the last 40% of the chord. This is followed by the appearance of a very large and thick bubble at $t = 6.5$ whose shape is swept in the downwind direction. The top surface pressure distribution is such that the aerofoil experiences a downward force causing a sharp fall of pitching moment. The bursting of the bubble at $t = 6.5$ alters the streamline curvature on the lower surface favourably due to the presence of a

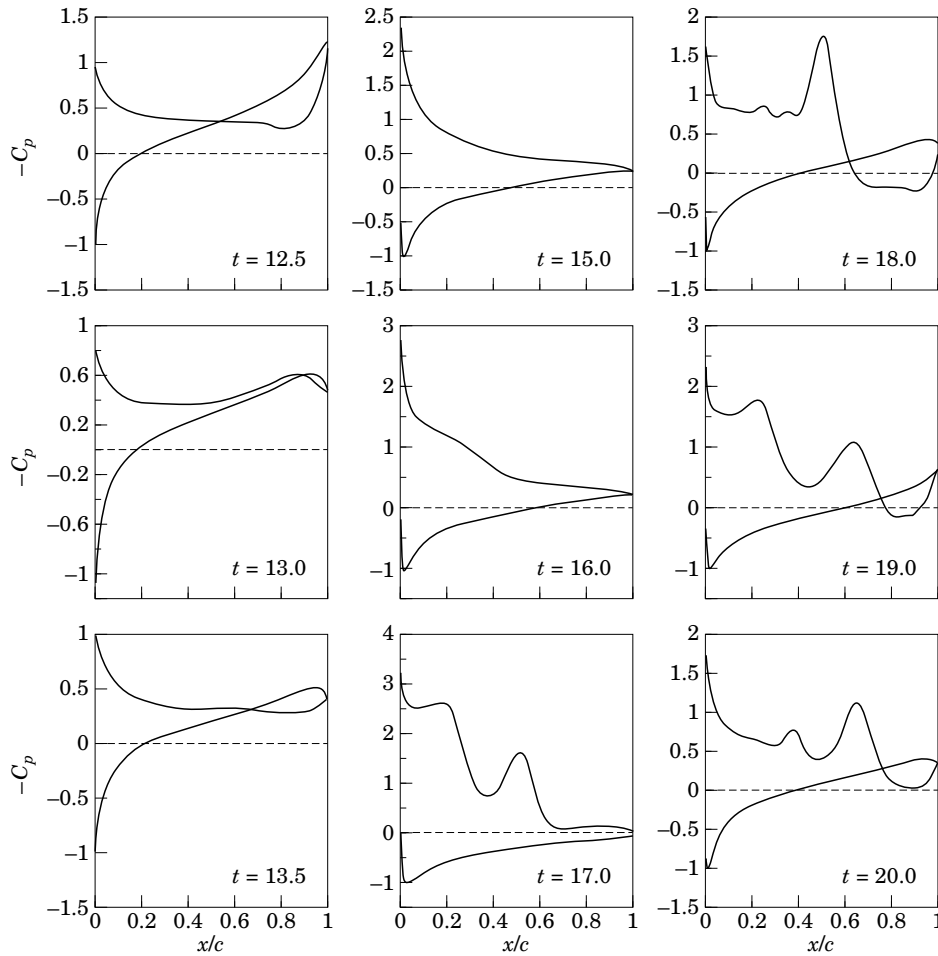


Figure 6(b). (Continued.)

detached vortex right over the trailing edge. For this flow case the convection dominates, and it can be seen that the vortices do move away from the body quickly once they are released, implying large temporal gradients and stretched longer vortices in the near wake.

At $t = 7.0$ the flow is separated near the trailing edge, and there are no bubbles on the aerofoil; the increase in lift is due to the detached vortex near the trailing edge. This vortex induces a suction over the top surface and prevents flow acceleration on the lower surface. The subsequent downstream movement of this vortex at $t = 7.5$ leads to the formation of an alleyway. At $t = 8.0$ we notice the evolution of a mushroom-shaped bubble near the trailing edge, visible in the vorticity contour plot. This bubble forces the rear stagnation streamline to be at the trailing edge, increasing lift and pitching moment. The flow leaves the trailing edge smoothly, causing lower surface pressure reorganization. This situation continues till $t = 9.0$, when this second bubble merges with the rear stagnation point and the leading edge bubble grows. The growth is restricted, though, by the presence of the rear stagnation point upstream of trailing edge on top surface.

Beyond $t = 10.0$ the free vortex moves away while the trailing edge bubble increases in size, and by $t = 11.0$ another alleyway is seen to form. At $t = 11.5$ a free vortex near

the two-third chordwise location rotates in the anticlockwise direction creating a local suction peak. This vortex increases in size while moving downstream and squeezes the vortex near the trailing edge. This accounts for the increase in the pitching moment, while the lift does not increase appreciably. The downwind motion of the vortex pair causes the formation of an alleyway causing the strong increase in lower surface pressure in such a way that there is a downward force in the rear half of the aerofoil. At $t = 13.0$ the increase in lift and pitching moment is associated with the appearance of another mushroom-shaped bubble near the trailing edge top surface. The dip in the value of lift at $t = 13.5$ is due to weak alleyway formation. From this time onward, up to $t = 16.0$, the lift and pitching moment increase as during the events from $t = 7.5$ to $t = 9.0$. Further increase in lift from $t = 16.0$ to $t = 17.0$ is due to the location of the rear stagnation point near the trailing edge.

Following $t = 17.0$, there are two bubbles near the leading edge, both of which provide a suction locally and create flow deceleration over the aerofoil between these vortices. These vortices migrate downstream and the rear one moves off the surface, so that a negative lift is produced in the rear half of the aerofoil at $t = 18.0$. Subsequently, one can notice multiple bubble formation on the surface. The relative insensitivity of the drag value with time for this case is simply due to the fact that the body behaves like a streamlined body, although the flow is weakly unsteady during this interval. Additionally, one can observe elongated structures in the vorticity plots at $t = 8.0$ consisting of vortices of the same sign. These structures distort and form necks due to self- and mutual interference, which leads to tearing of these structures into smaller vortices. These disintegrated vortices diffuse quickly, as can be seen in the vorticity plots at $t = 10.0$, 11.0 and 11.5 .

5.3. CASE 3: $Re = 3\,000$, $t/c = 0.1$ AND $\alpha = 12^\circ$

For this case the vorticity and C_p distributions are shown in Figures 7(a) and 7(b). This case is qualitatively similar to the $\alpha = 10^\circ$ case in the initial phase, except for a slightly higher lift.

Here the leading edge bubble forms earlier and can be seen at $t = 1.0$, because of the larger pressure gradient encountered by the flow as compared to the $\alpha = 10^\circ$ case. Additionally, a secondary bubble is seen at $t = 3.0$ which grows and interacts with the primary bubble; as a result of this, the reattachment point of the primary bubble shifts rearward till it merges with the rear stagnation streamline at around $t = 4.5$. Between $t = 5.0$ and $t = 5.5$ another bubble forms at the leading edge, which has the shape of a backward-facing step because of the presence of a free vortex on top of the trailing edge. The induced effect reduces the suction surface pressure and the strong curvature of the streamlines on the lower surface locally accelerates the flow. The acceleration is so rapid that there is, in fact, a very strong suction at the lower surface near trailing edge (as seen from the C_p plot at $t = 6.0$). The same sequence of events in the neighbourhood of the trailing edge occurs at $t = 7.5$, 9.5 and 11.0 when the aft part of the aerofoil experiences a downward force. The alleyway formation is present in this case also, but it causes lesser streamline curvature as compared to the $\alpha = 10^\circ$ case. Between $t = 12.0$ and $t = 13.5$ the rear stagnation streamline moves on the top surface near the trailing edge, while a bubble forms on the top surface which grows with time. The appearance of this leading-edge bubble accounts for the steady increase in lift. Once the rear stagnation streamline settles at the trailing edge, the lift continues to increase with time till $t = 15.0$, where one can see a secondary bubble—the situation being analogous to that at $t = 4.0$.

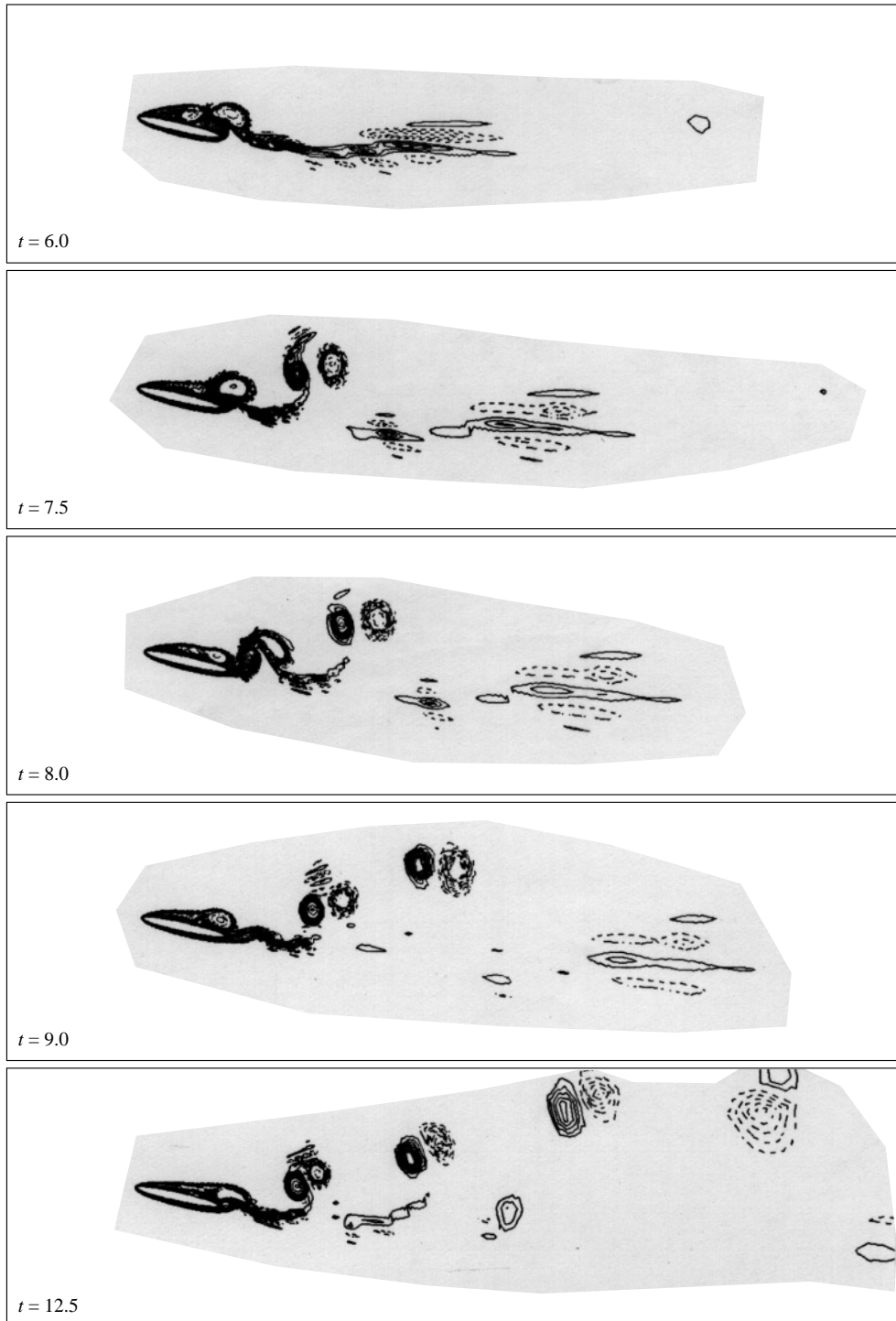


Figure 7(a). Vorticity contours for the case of $t/c = 0.1$, $Re = 3000$ and $\alpha = 12^\circ$ at times indicated in the figures.

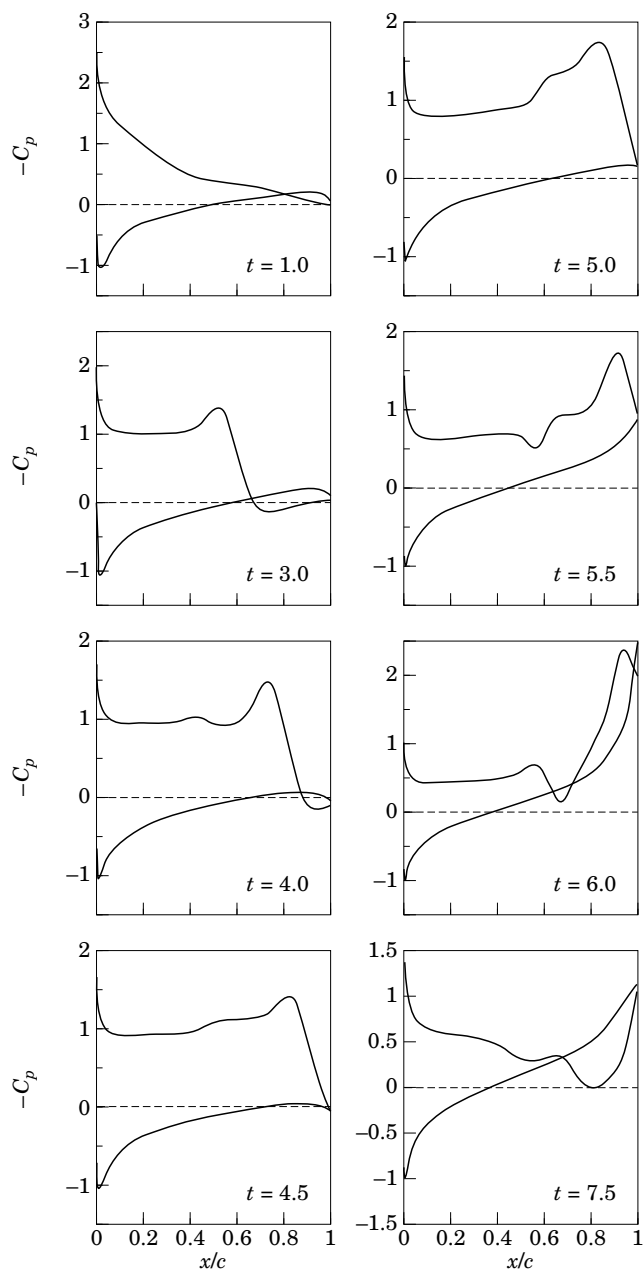


Figure 7(b). (Continued.)

Looking at the vorticity contour plots in Figure 7(a), we can notice some interesting phenomena, one of which is the very elongated vortex structures in the near wake at early times. This is due to the predominance of convection over diffusion and is different from what has been observed in Nair & Sengupta (1996) for the zero angle of attack case. For the zero angle of attack case this is associated with the long bubble formation in the near wake which originates near the trailing edge. This pair of vortices grow in length with the bubble and hence have smaller convection speed. It was also shown that such a bubble breaks down as a consequence of Kelvin-Helmholtz

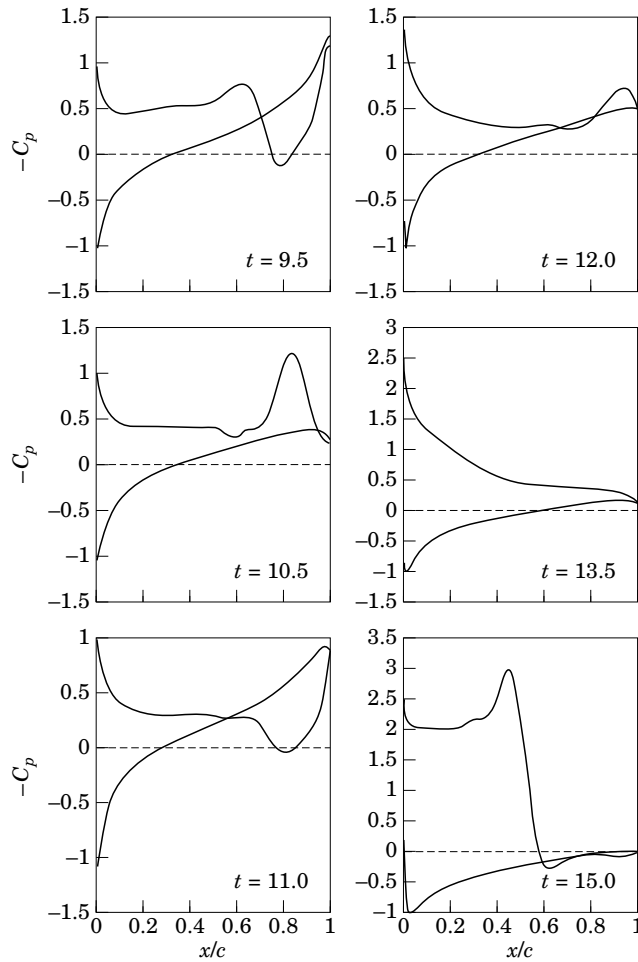


Figure 7(b). (Continued.)

instability into smaller vortices. Comparatively, no such instability is seen to occur here, but the strain rates in the streamwise direction are so large that eventually the elongated vortex starts tearing up. Beginning at $t = 6.0$ we notice the neck formation in the elongated structure. This elongated structure contains smaller co-rotating vortices. Tearing occurs at $t = 7.5$, 8.0 and 12.5 . It should be noticed that, after this elongated structure migrates out of the frame, no such similar events occur. Furthermore, after $t = 7.0$ one can see the distinct rolling of the vortex sheet in the near wake to form strong vortices. The shed vortices are of alternate signs and are seen to form pairs. Significant vortex pairing is seen to occur at $t = 8.0$, 9.0 , 11.0 and $t = 12.5$ in a sequence. These vortex pairs display interesting dynamics: they convect downstream while rotating about each other. Barring the first pair, the subsequent three pairs rotate counter-clockwise. Inspecting Figure 8, we can see that the overall loads and the moment have a qualitative similarity at these times with the $\alpha = 10^\circ$ case.

5.4. CASE 4: $\text{Re} = 10\,000$, $t/c = 0.25$ AND $\alpha = 30^\circ$

This particular case is computed for investigating the effects of Reynolds number and the t/c ratio. Figures 9(a), 9(b) and 9(c) show the stream function, vorticity and

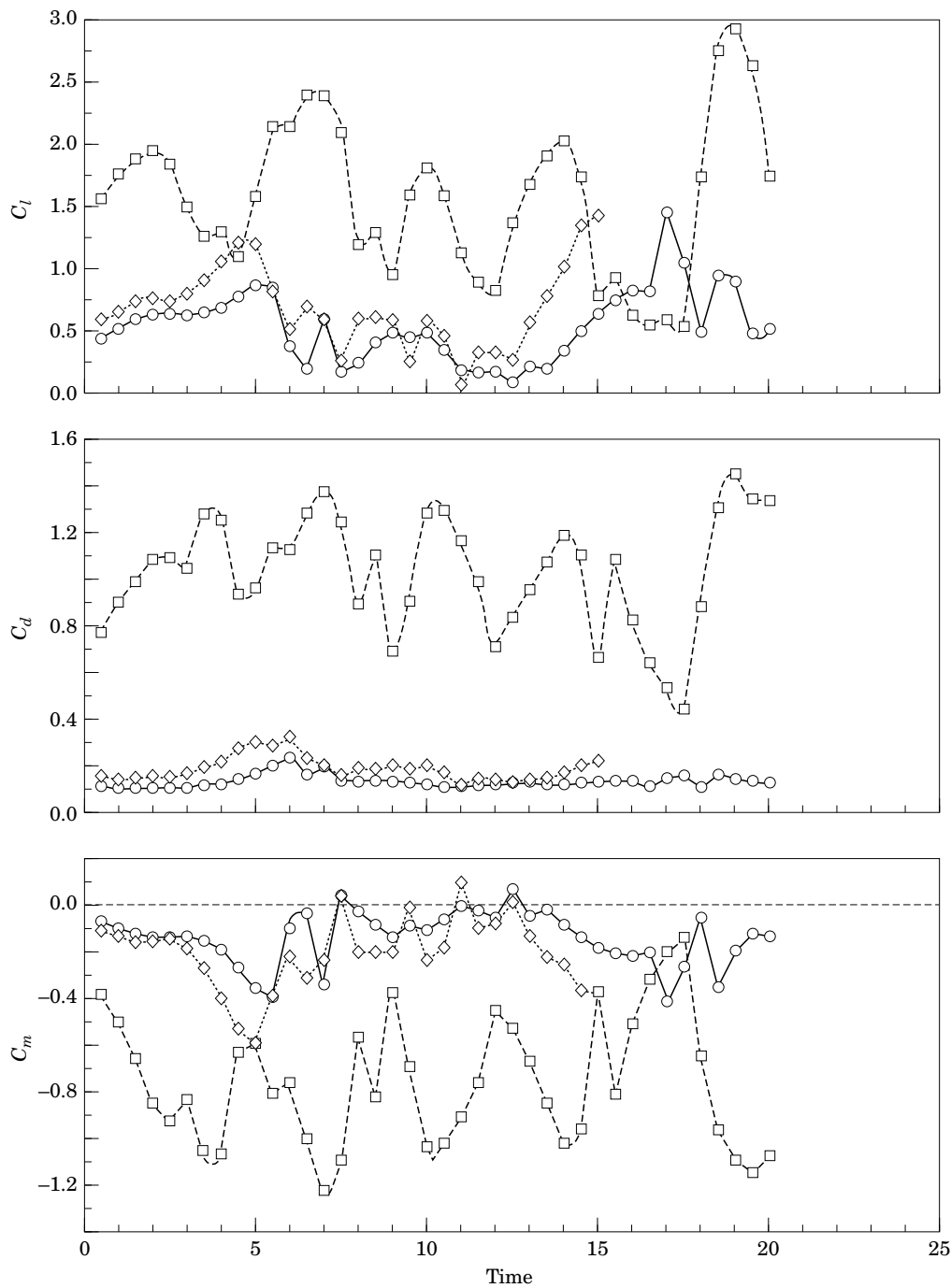


Figure 8. The integrated loads and moment for the cases of Figures 4, 6 and 7: (a) lift; (b) drag; (c) pitching moment. (○) $\alpha = 10^\circ$; (◇) $\alpha = 12^\circ$; (□) $\alpha = 30^\circ$.

pressure contours, respectively. Figure 11 shows the variation of loads and moment as a function of time for both $\alpha = 10^\circ$ and 30° at $Re = 10\,000$.

In this case also one can notice the formation of trailing-edge bubble very early on. Additional bubbles form near the leading edge, within which multiple vortices can be

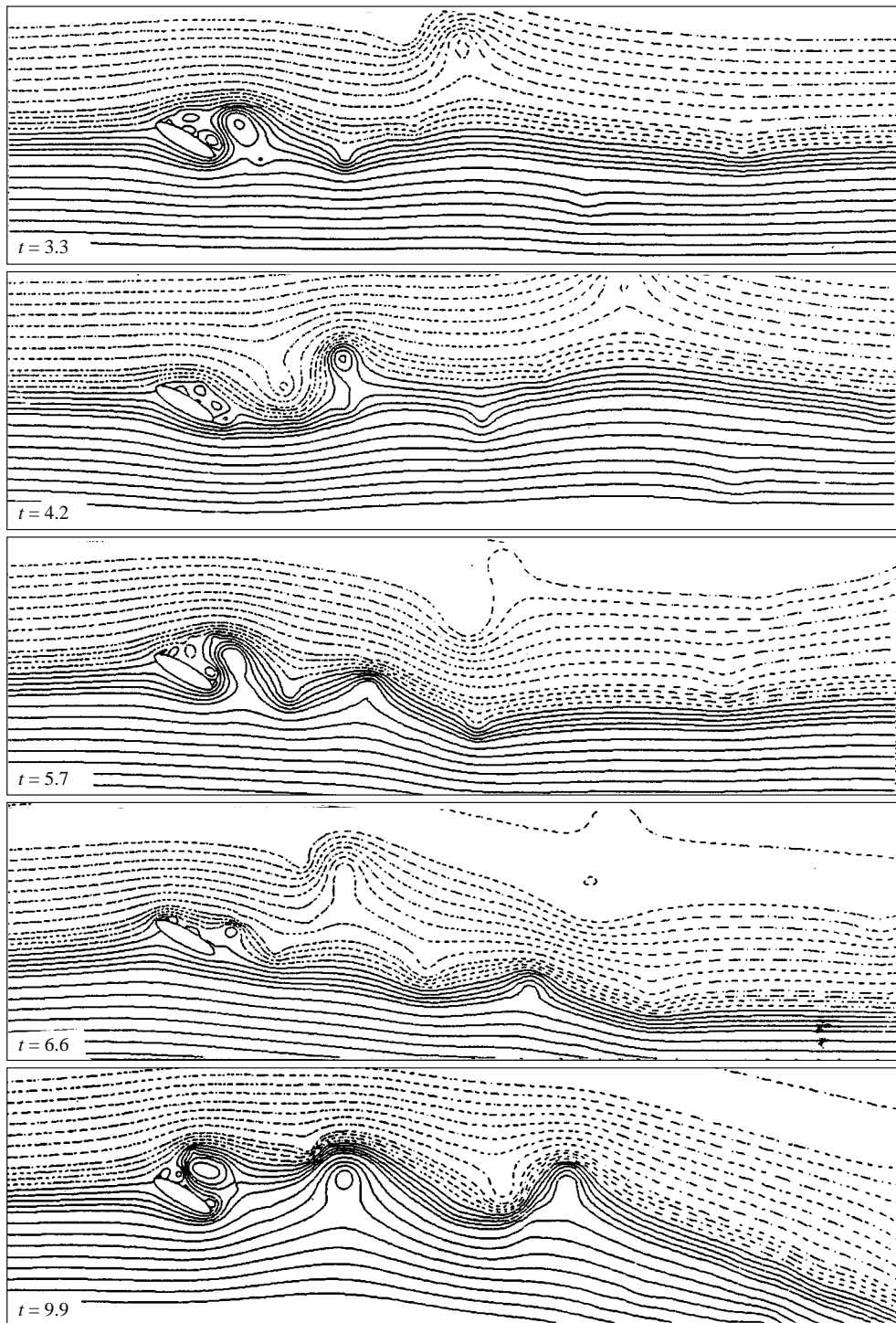


Figure 9(a). Streamline contours for an elliptic cylinder of $t/c = 0.25$, $Re = 10\,000$ and $\alpha = 30^\circ$ at times indicated in the figures.

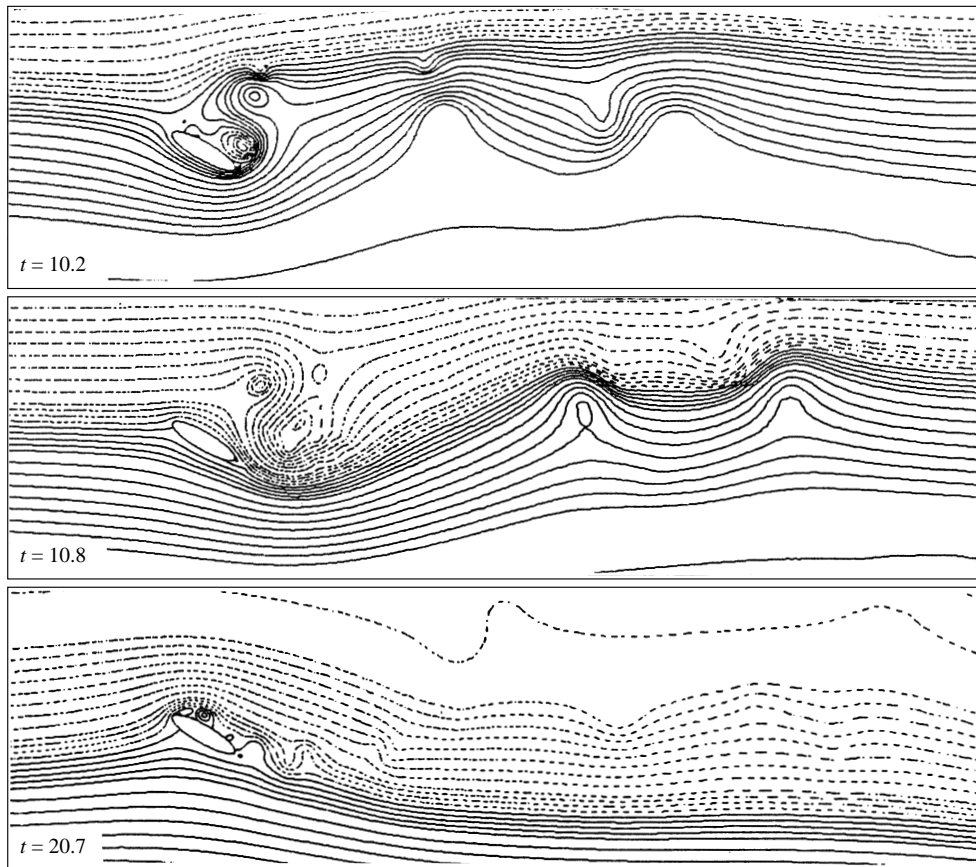


Figure 9(a). (Continued.)

traced. For this case, bubbles are always present on the top surface, which is responsible for high values of lift. There are time instants when drag is significantly higher than lift, e.g. at $t = 1.8, 3.0, 3.3, 5.7$ and 9.9 . At $t = 10.2$ the drag is high while the lift attains a negative value. Only at $t = 10.8$ are there no bubbles on the top surface, but the high value of lift is due to the induced effects of the detached vortices near the trailing edge. Overall, the large swing of lift is due to the rapid movement of front and rear stagnation points from the top to bottom surface; this can be seen in the stream function contour plots between $t = 9.6$ to $t = 10.8$. This also causes the whole wake to swing during the same period. The vorticity and pressure contours in Figure 9(d) show that there is an increase in the number of vortices that are shed into the wake. These shed vortices interact in pairs of two and three in the wake, as can be seen clearly from the pressure contours, causing the wake to swing.

Another important feature to be noticed is the movement of the front stagnation point on the ellipse. As the wake is deflected upwards, the front stagnation point moves toward the leading edge (closer to the upper surface) and is deflected downwards when the front stagnation point moves away from the leading edge. The C_p distribution beyond $t = 5.4$ on the body behaves more or less similarly to earlier times, except that the front stagnation point movement and the time derivative of lift change sign rapidly compared to the early stages. From $t = 6.6$ to $t = 7.5$ there are no large and strong vortices shed into the wake. Once again, from $t = 7.8$ onwards strong vortices are shed

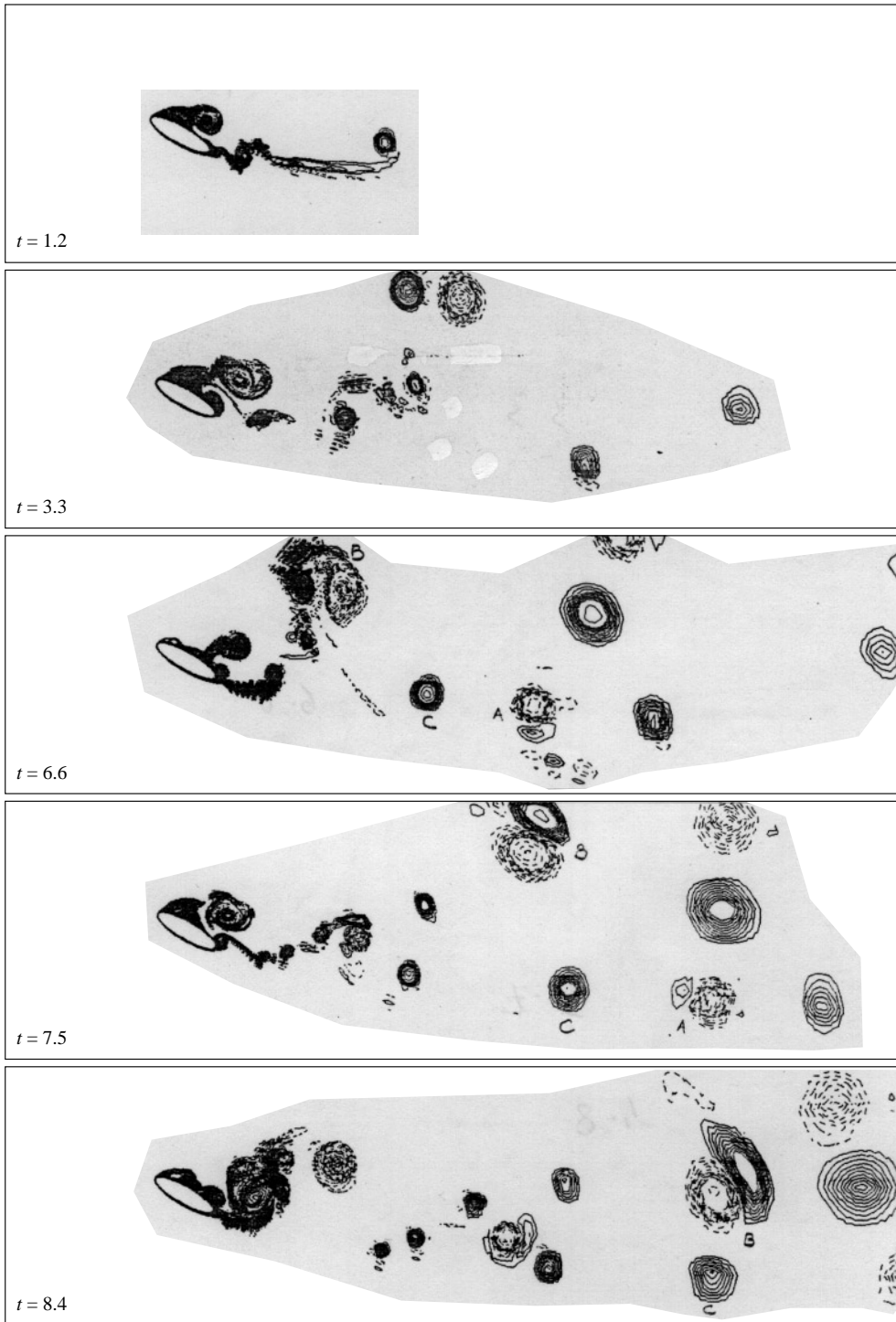


Figure 9(b). Vorticity contours for the case of $t/c = 0.25$, $Re = 10000$ and $\alpha = 30^\circ$ at times indicated in the figures.

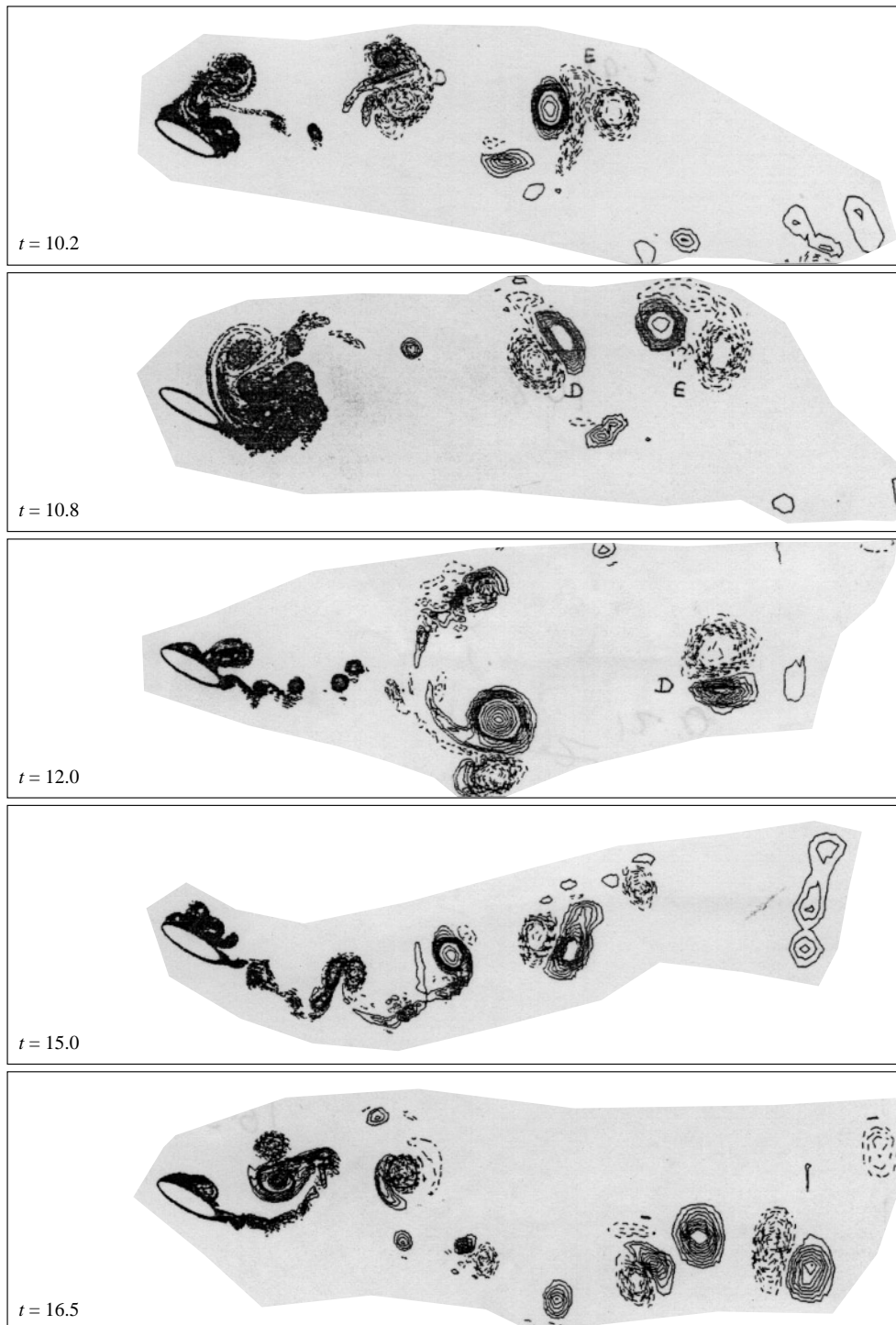


Figure 9(b). (Continued.)

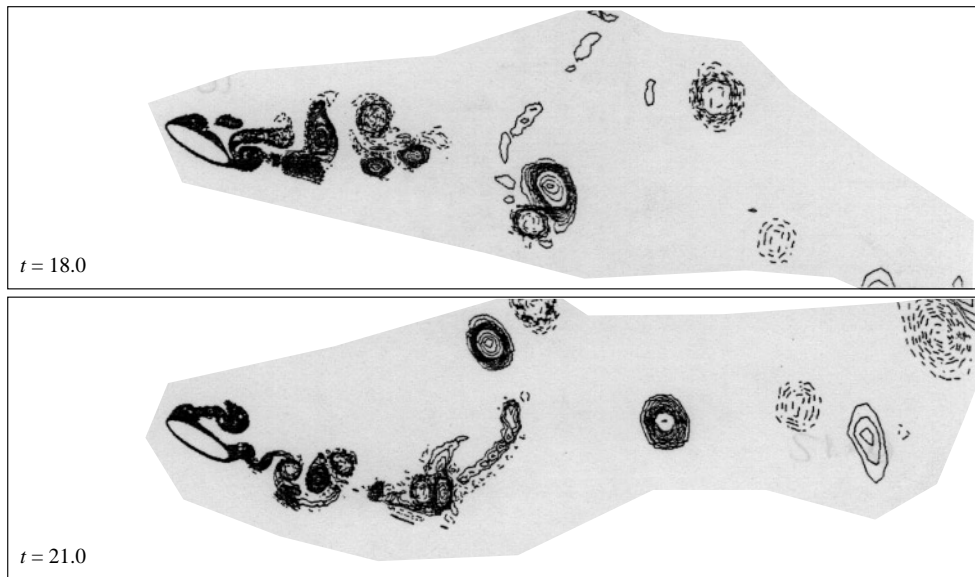


Figure 9(b). (Continued.)

into the wake in pairs, which start interacting with each other as can be seen from the pressure and vorticity contours. This again results in deflection of the wake and movement of the front stagnation point. It is to be noted that there is strong downward deflection of the wake starting from $t = 8.4$, followed by an upward deflection after $t = 9.9$. An interesting case occurs at $t = 10.2$, when the front stagnation point has moved off the body. During this deflection of the wake, the front stagnation moves from the lower surface to the upper surface, resulting in a suction in the lower surface. From the streamline plots it can be noticed that at $t = 10.2$ there is no half saddle point near the leading edge of the aerofoil. Instead there is a full saddle point over the aerofoil near the leading edge, off the body, indicating unsteady separation. The C_p distribution demonstrates this too, as there are no maxima over the top surface. Here we see long bubbles of large transverse extent, and within these bubbles there is more than one smaller vortex—as seen in streamline contours at $t = 4.2, 8.4, 11.4$ and 17.4 . Also, multiple bubbles form on the top surface at $t = 1.2, 3.3, 7.5, 14.7$ and 20.7 . At $t = 1.2, 14.7$ and 20.7 the various vortices have an additive lift, generating interference, while at $t = 3.3$ and 7.5 the position of the rearmost bubble gives rise to alleyway formation causing significant loss of lift due to flow acceleration on the lower surface. At the same time, flow separation from the leading edge causes flow deceleration on the top surface near leading edge.

A vortex pair sheds at $t = 10.5$ and subsequently undergoes strong interaction. The wake starts an upswing at $t = 11.4$, which causes the front stagnation point to move on the upper surface and a strong suction on the lower surface. After $t = 12.3$ and till $t = 21.0$ (the limit to which the computations were performed), vortices are shed continuously in the wake and they are more or less equispaced. The other important point is that the deflection of the wake is determined by the direction of rotation of this interacting pair. For a clockwise rotation of the pair, the wake deflects downwards and the stagnation point moves towards the trailing edge on the lower surface and *vice versa*. This can be clearly seen by comparing the pressure and stream function contours.

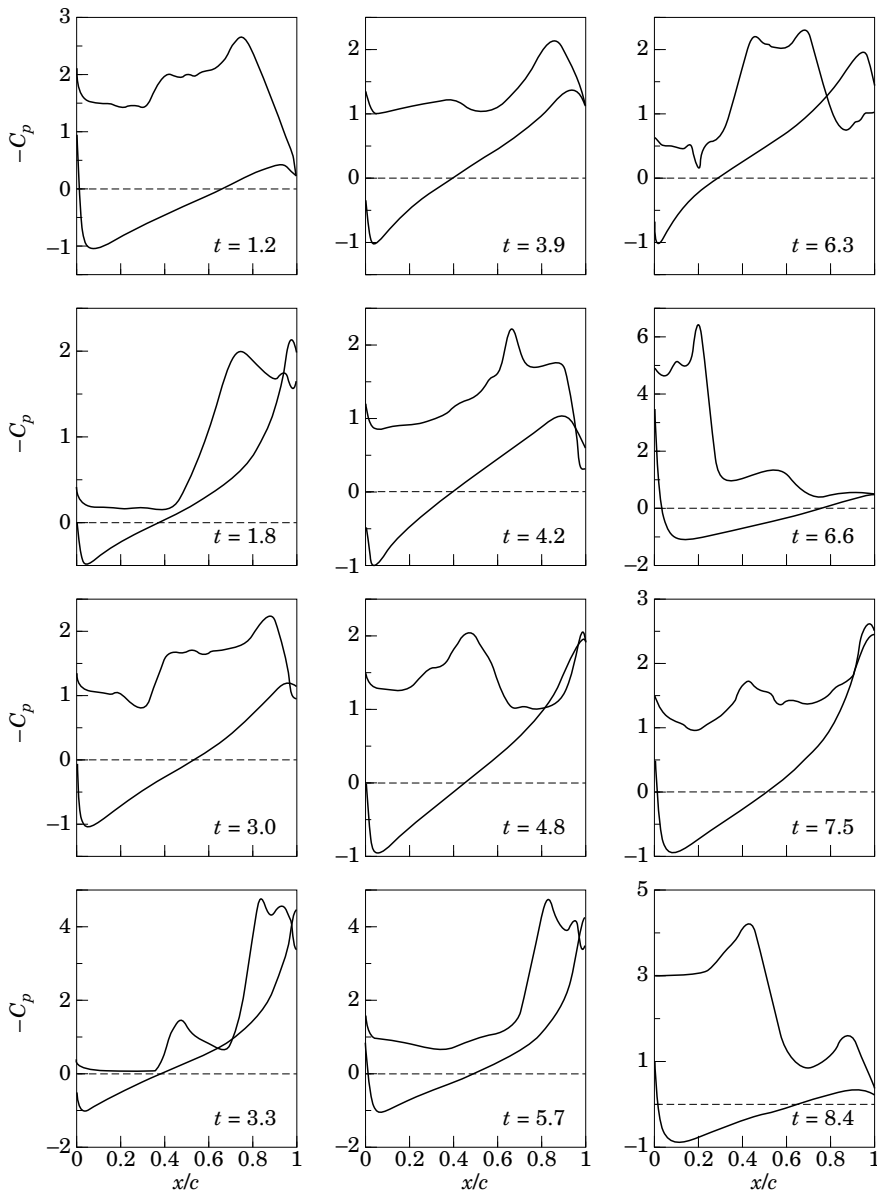


Figure 9(c). C_p distribution for the case of $t/c = 0.25$, $Re = 10\,000$ and $\alpha = 30^\circ$.

The near wake also exhibits another interesting phenomenon. For an observer located at a fixed point in the wake, the arrival of vortices is intermittent. The events are reminiscent of transitional flows. This can be ascertained from the vorticity contour plots. For this case the first perceptive increased spacing between vortices can be located at one-and-a-half chords away from the trailing edge, at and beyond $t = 3.3$, and this spacing increases while the aggregate moves slowly downstream. A second event can be traced at $t > 7.5$, located three chords away from the trailing edge. A third event occurs at $t > 10.8$. This zone of activity and silence can be related to vortex pairing involving multiple vortices.

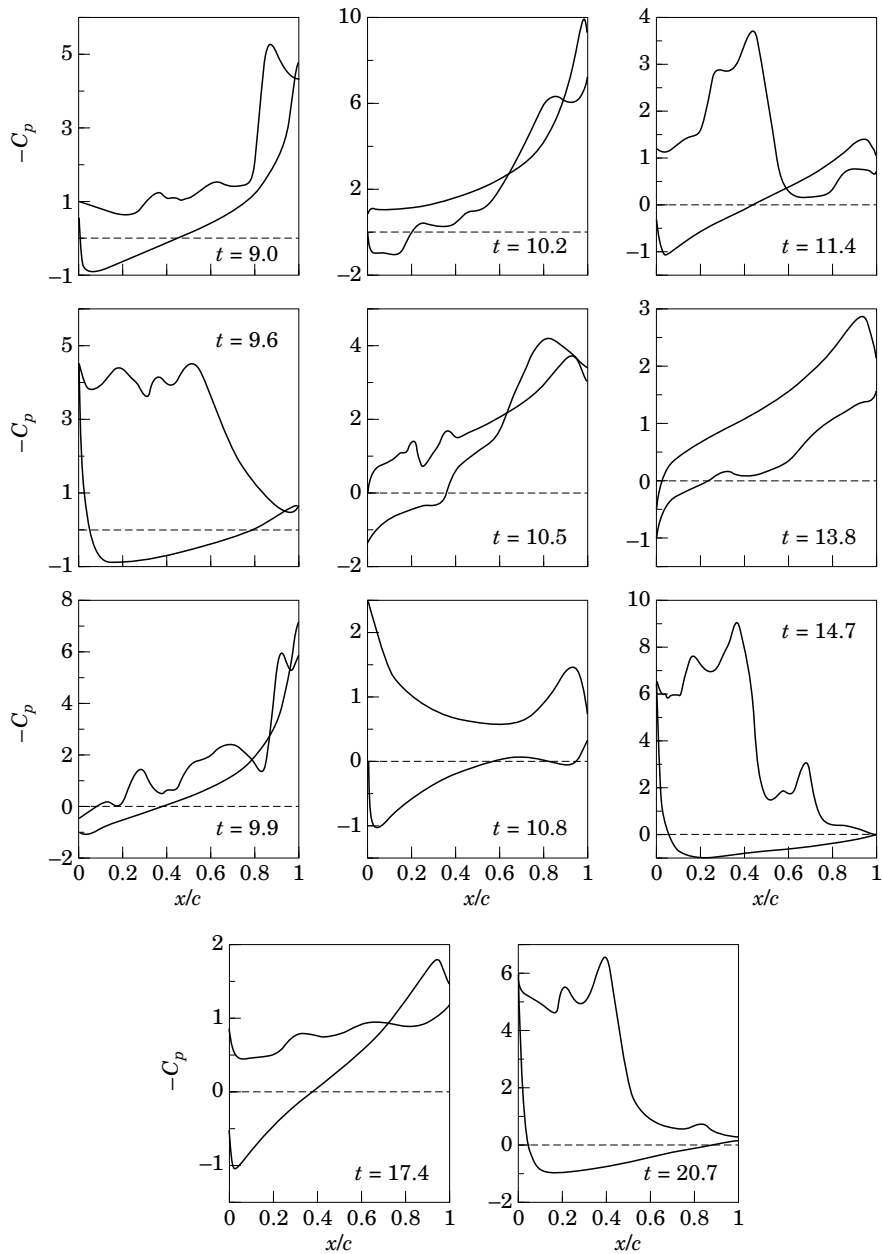


Figure 9(c). (Continued.)

5.5. CASE 5: $Re = 10\,000$, $t/c = 0.25$ AND $\alpha = 10^\circ$

For this case the stream function and vorticity contours are shown in Figures 10(a) and 10(b) respectively; also some surface pressure (C_p) plots are shown in Figure 10(c). Specifically, for this case the lift generated by the section is much lower than for the 30° case, with a smaller range of variation. Interestingly enough, the negative lift occurs more often and over longer duration than in the previous case. Although the front stagnation point does not move appreciably, the unsteady effects are solely due to the formation of bubbles over the top surface near the trailing edge and consequent flow

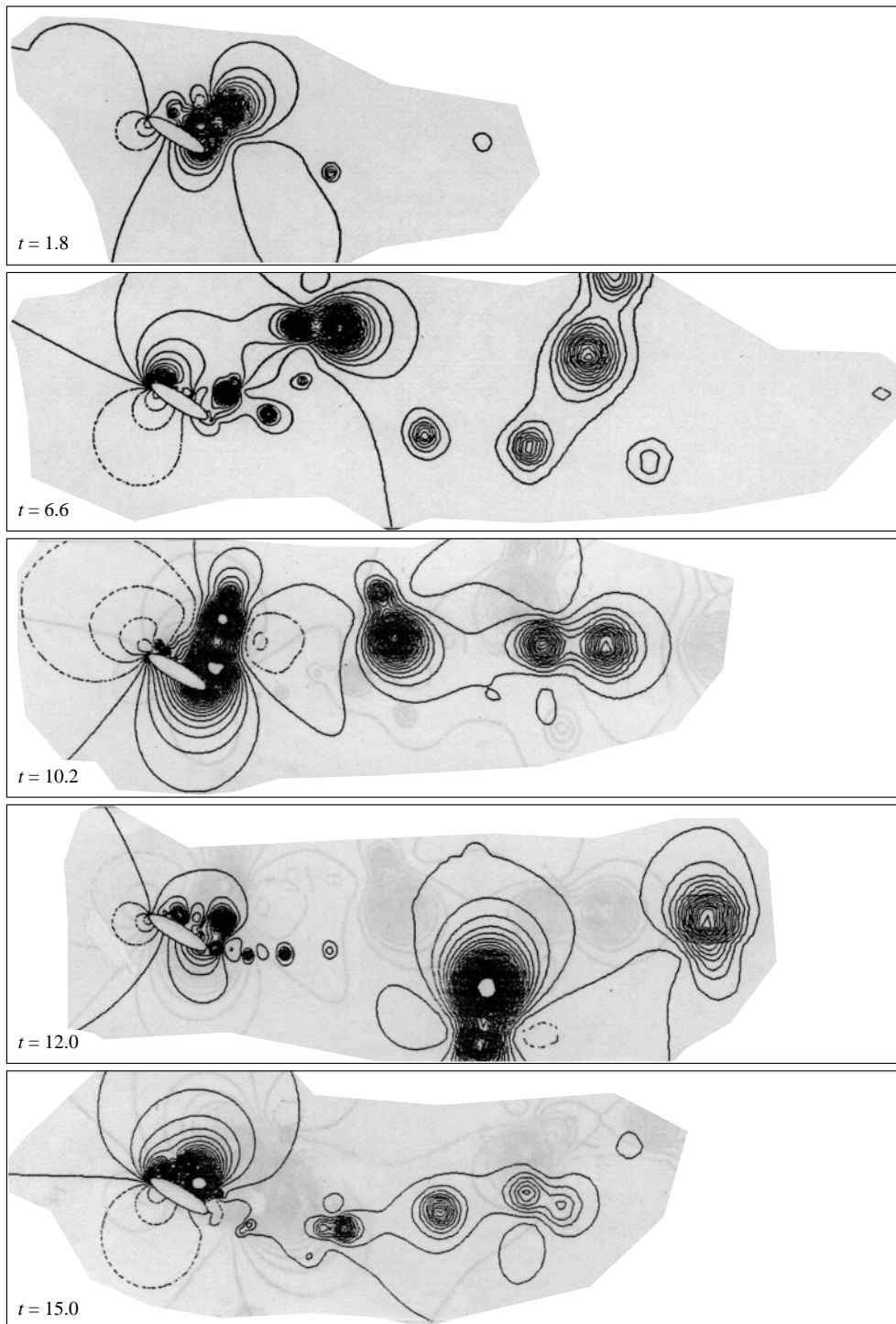


Figure 9(d). Pressure contours for the case of $t/c = 0.25$, $Re = 10\,000$ and $\alpha = 30^\circ$.

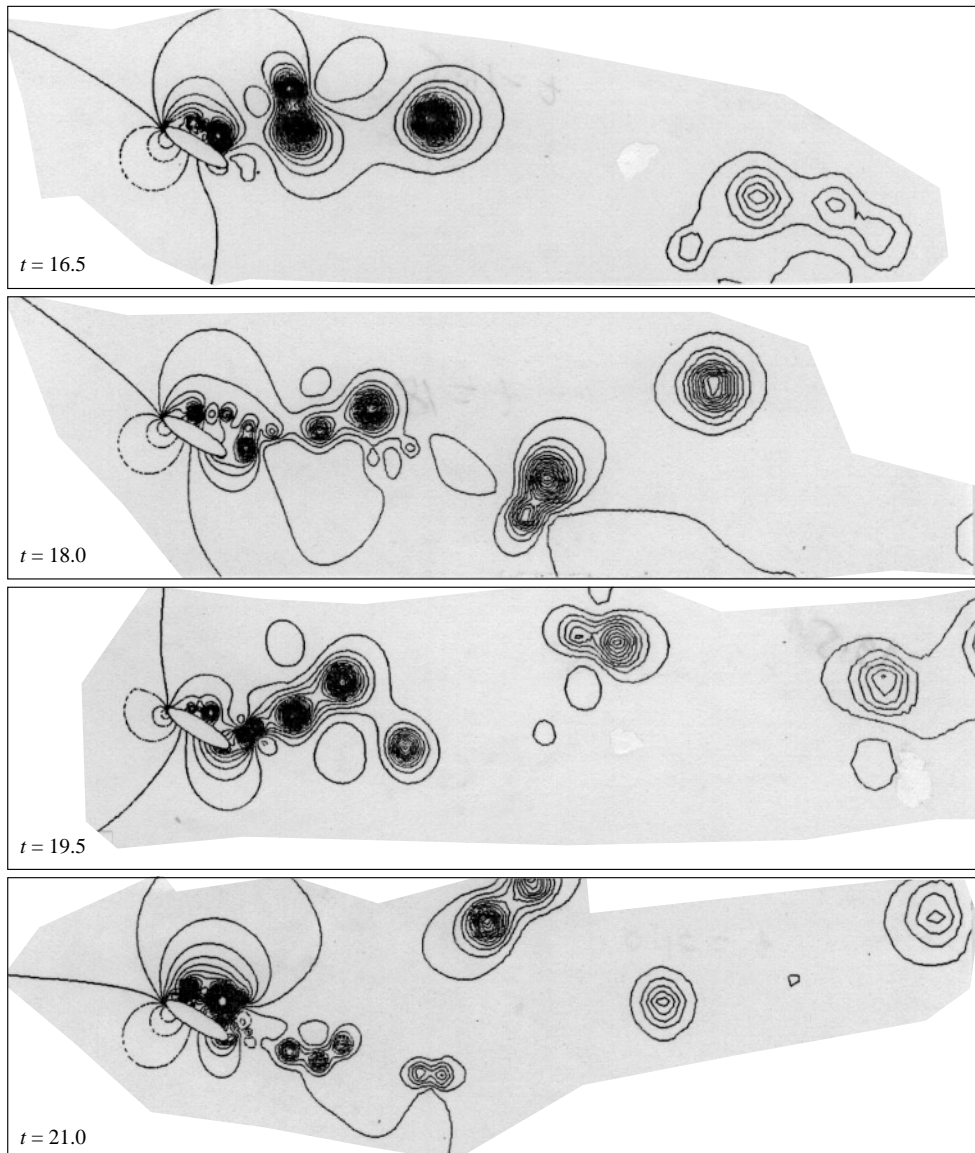


Figure 9(d). (Continued.)

acceleration over the lower surface. Because of the weakness of the vortices shed in the wake, the vortices do not exhibit strong coherence and suffer stronger diffusion as compared to the previous case. We also see that the zones of no vorticity are also fewer in number, and even when they do occur the length is smaller—which is a direct consequence of low vortex interaction in the wake. For the $\alpha = 30^\circ$ case we have noticed significant vortex interaction leading to doublet and triplet formation, which is responsible for the lengthening of the *zone of low activity*. Here the zones more or less form at the same location (at about 1.5 times the chord from the trailing edge) at discrete times (at $t = 4.2, 8.4, 10.2$ and 17.4). The lack of coherence of the shed vortices and stronger diffusion lead to multiple vortex interaction. One such interaction can be noticed at $t = 13.2$, which gives rise to very elongated vortex structure due to

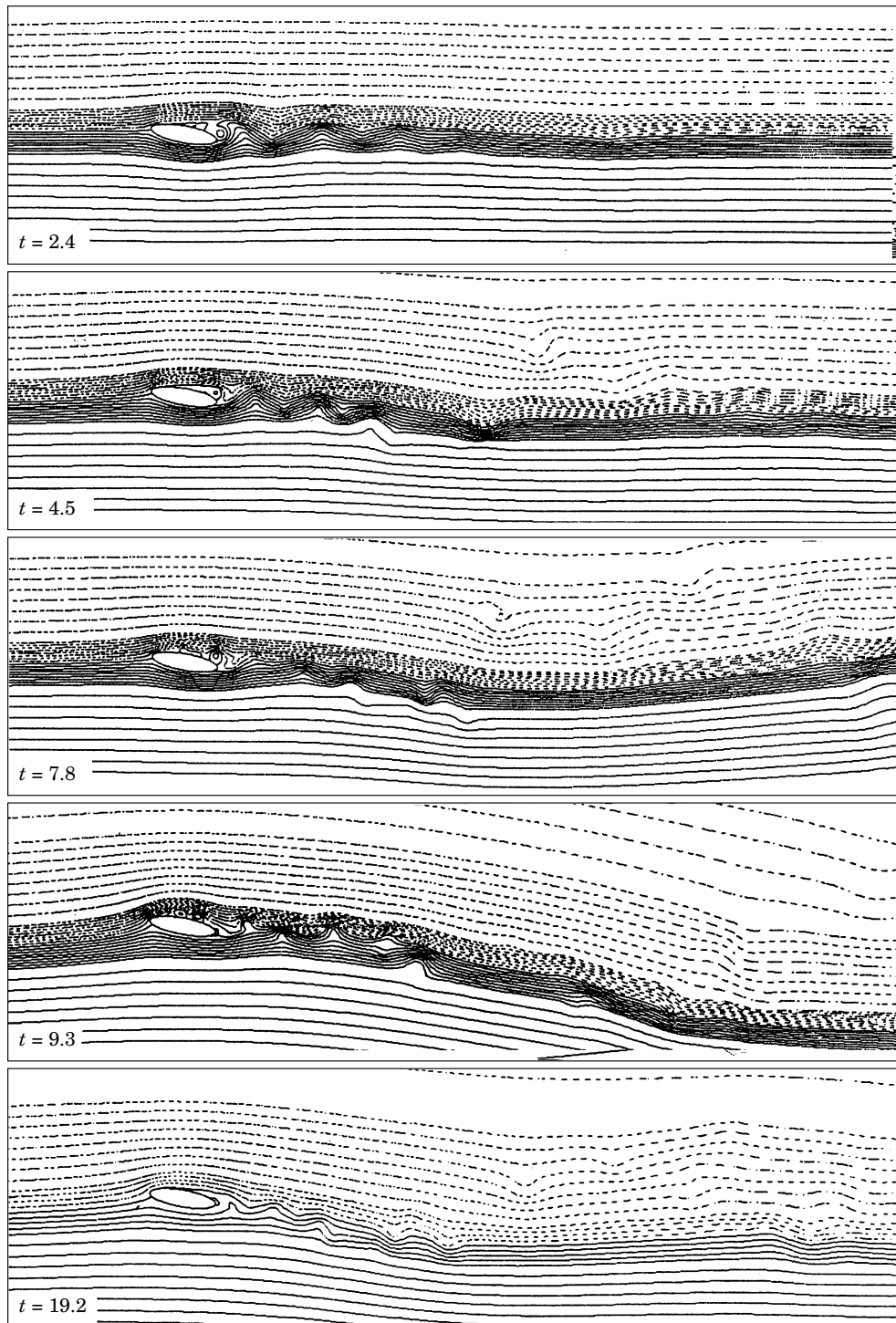


Figure 10(a). Streamline contours for an elliptic cylinder of $t/c = 0.25$, $Re = 10\,000$ and $\alpha = 10^\circ$ at times indicated in the figures.

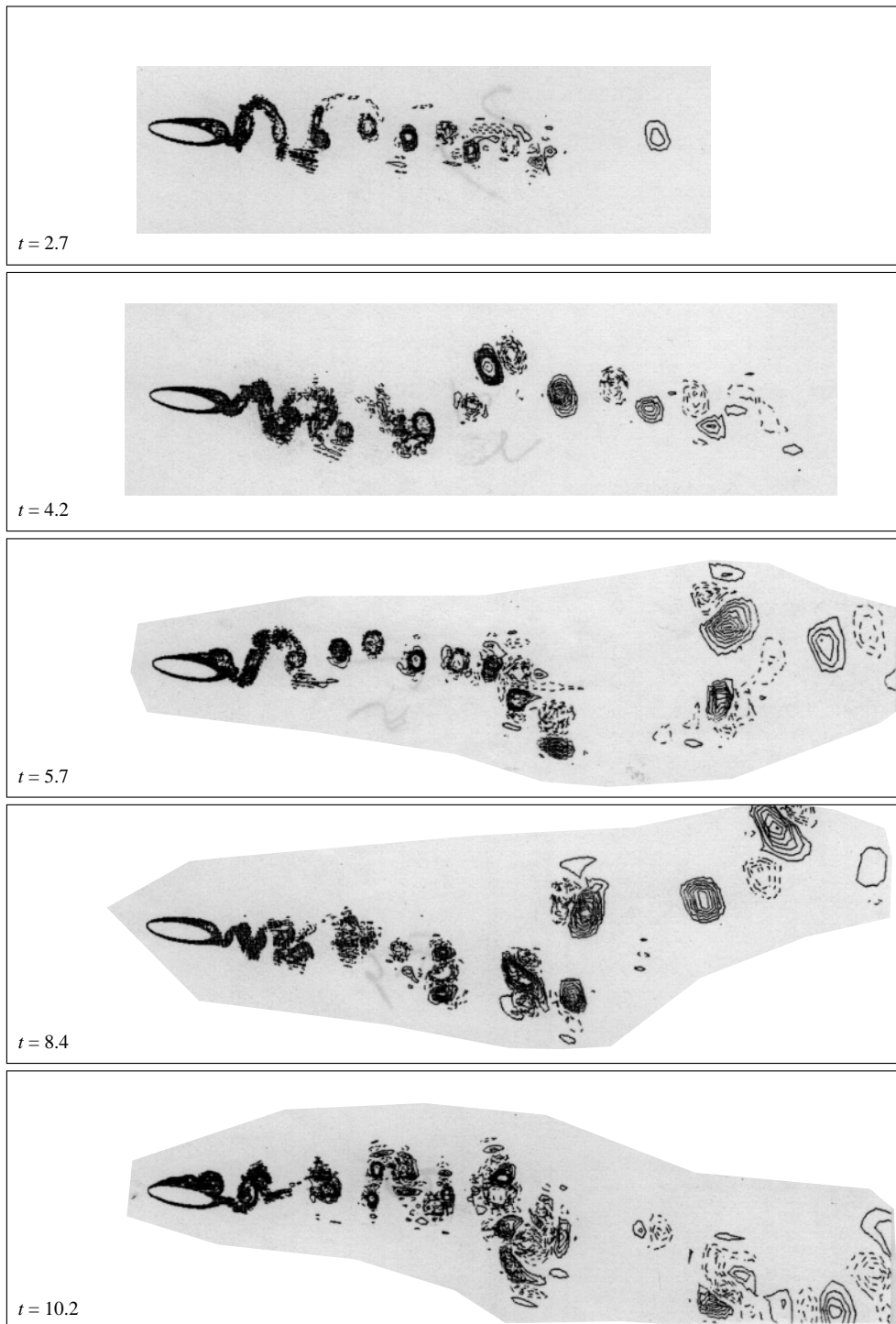


Figure 10(b). Vorticity contours for the case of $t/c = 0.25$, $Re = 10\,000$ and $\alpha = 10^\circ$ at times indicated in the figures.

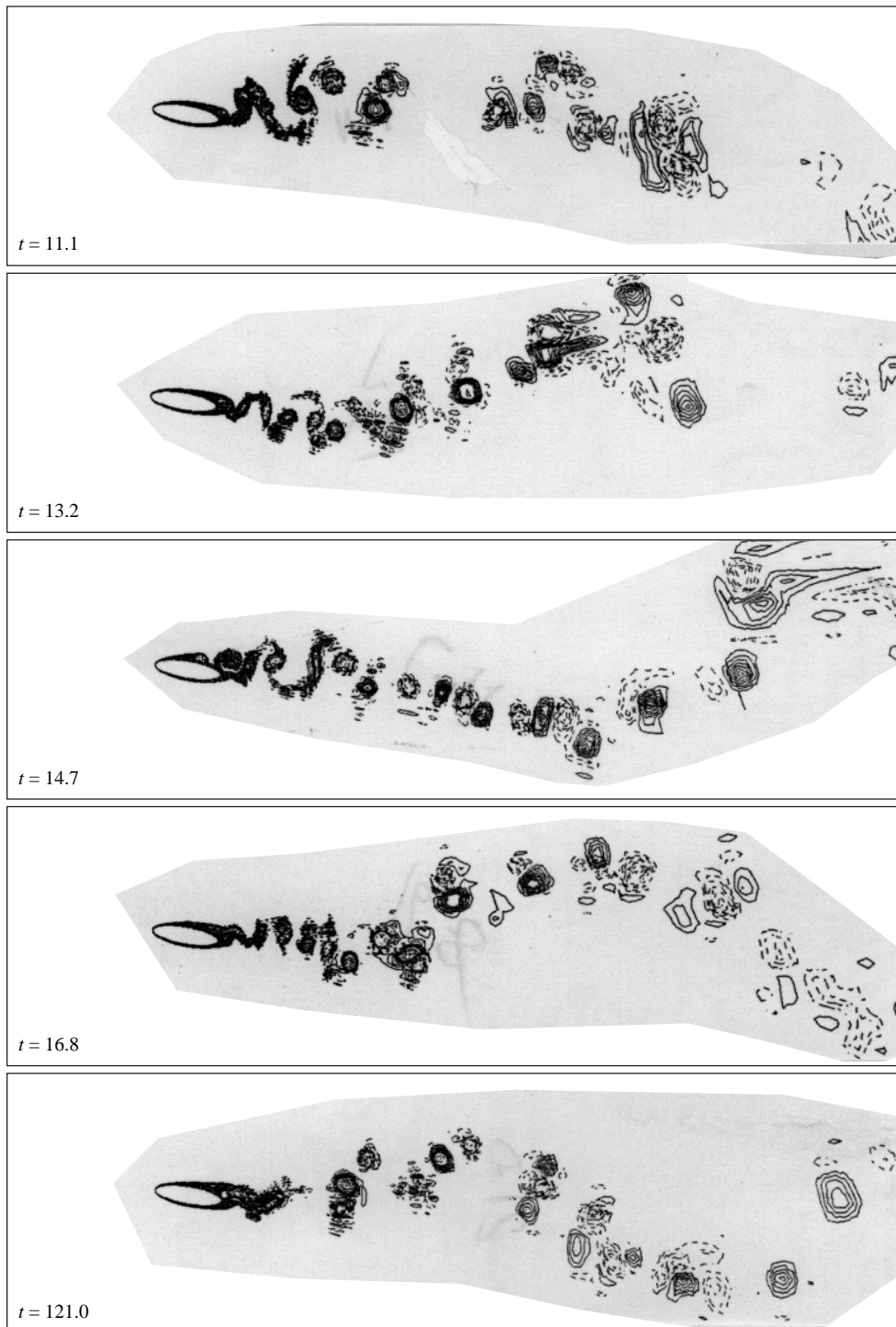


Figure 10(b). (Continued.)

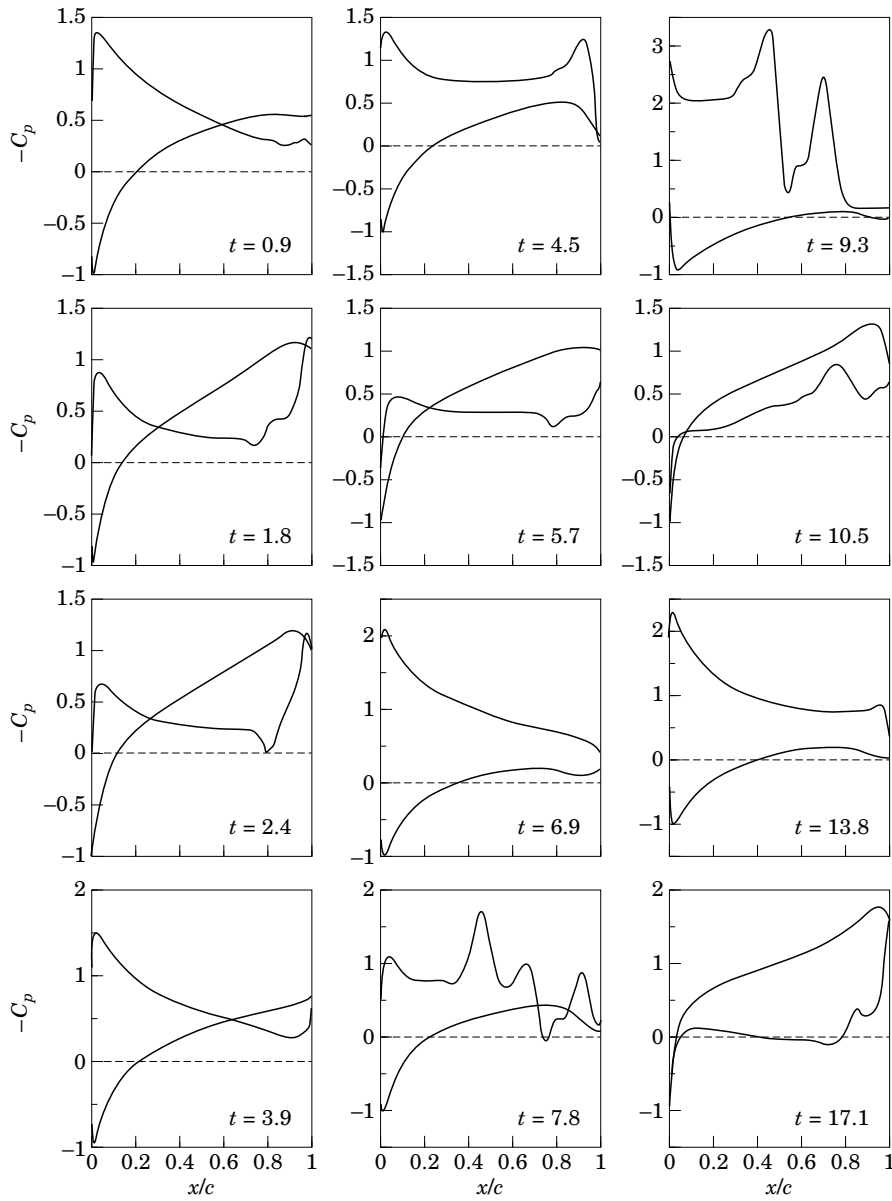


Figure 10(c). C_p distribution for the case of $t/c = 0.25$, $Re = 10\,000$ and $\alpha = 10^\circ$.

convection, and which eventually leads to tearing of vortices in the wake as they convect downstream.

5.6. EFFECT OF THE ANGLE OF ATTACK

5.6.1 $t/c = 0.1$, $Re = 3\,000$

Referring to the early-time results in Figures 4(a), 6(a) and 7(a) it can be noted that for smaller angles of attack the separation first starts from the trailing edge and moves upstream. A small leading edge bubble is formed which grows in size and forms a long

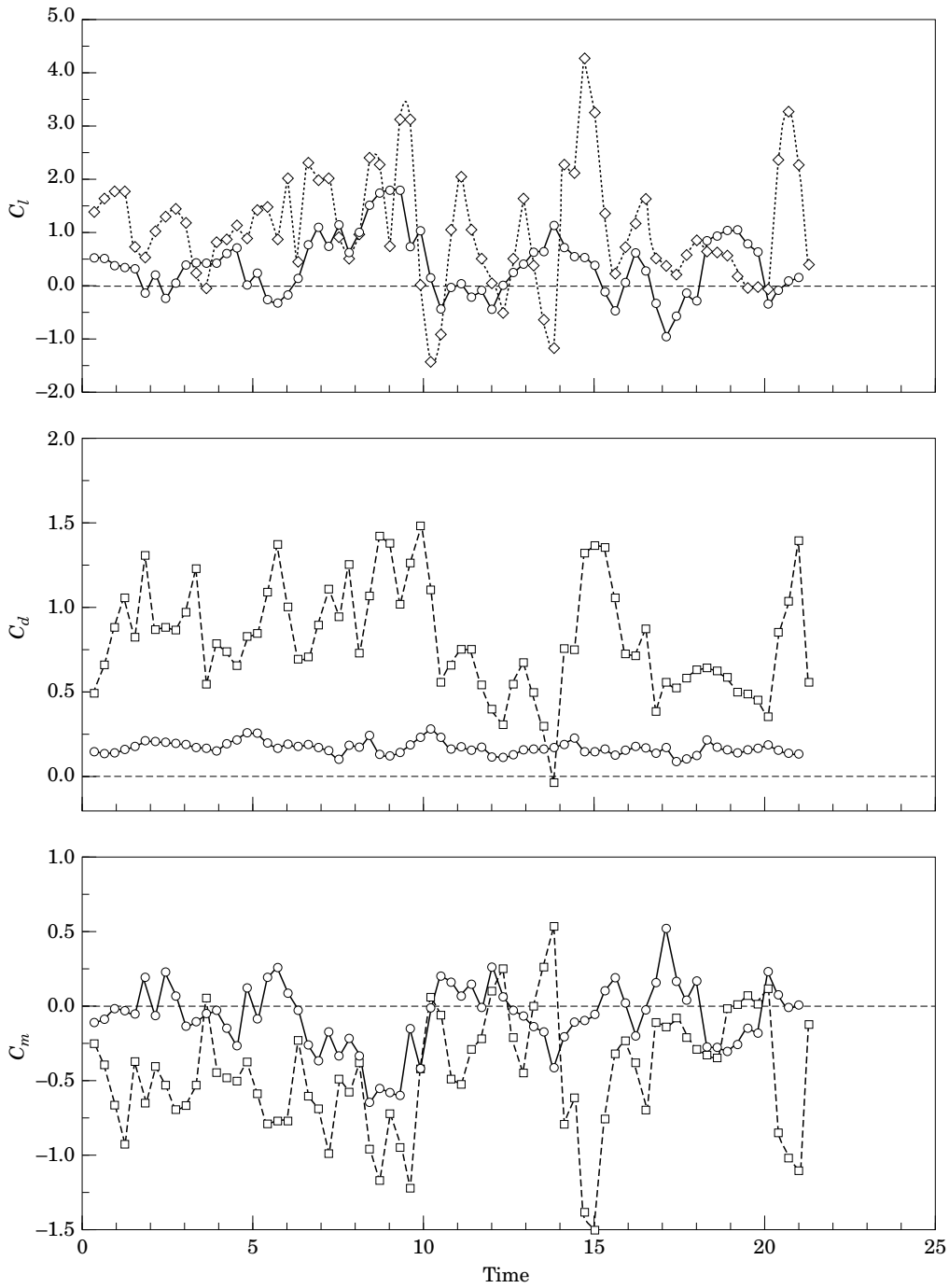


Figure 11. The integrated loads and moments for the cases of Figures 9 and 10: (a) lift; (b) drag; and (c) pitching moment. (○) $\alpha = 10^\circ$; (□) $\alpha = 30^\circ$.

bubble for $\alpha = 10^\circ$. For $\alpha = 12^\circ$ this leading-edge bubble grows faster as compared to the previous case, but it breaks down into smaller bubbles sooner. For $\alpha = 30^\circ$ the leading-edge separation and bubble formation give rise to higher lift at the beginning. For $\alpha = 10^\circ$ and $\alpha = 12^\circ$, it is the leading-edge bubble which grows in size and breaks

down into smaller ones before convecting downstream. Secondary vortices created, due to the adverse pressure gradient, by the existing vortices are either absent or even if they are formed are weak, whereas for the $\alpha = 30^\circ$ case strong secondary vortices are formed, as can be noted from Figure 4(a). The strength of the vortices increase with α , resulting in strong vortex interactions. This causes an increase in the front stagnation point movement and the deflection of the wake. Referring to the C_p distribution for the three cases, it can be said that peak in C_p value is higher for higher α , which is expected since stronger vortices are convected over the suction surface. This higher C_p causes a higher average lift. The average drag, moment and their fluctuations also increase with α .

5.6.2. $t/c = 0.25$; $Re = 10\,000$

Referring to the results in Figures 9(a) and 10(a), it can again be said that for smaller angles of attack the separation first starts from the trailing edge. Formation of a leading edge bubble is nearly absent for $\alpha = 10^\circ$, which can also be noted from the C_p plot, since there is no excessive peak in C_p at the leading edge. The secondary vortex formation is not significant for $\alpha = 10^\circ$, whereas for $\alpha = 30^\circ$ secondary vortices have a significant impact on the loads as well as vortex interactions in the wake. Strong vortices are formed for both cases, their strength increasing with the angle of attack. Observations regarding the front stagnation point movement, wake deflections and loads are similar to those for $t/c = 0.1$.

5.7. EFFECT OF t/c AND REYNOLDS NUMBER

Comparing the two t/c ratio cases, it can be seen that for $t/c = 0.1$ the flow behaves more like that over a conventional aerofoil. The separation point which is near the leading edge for $t/c = 0.1$ is either absent or is located further downstream for $t/c = 0.25$. The number and strength of the secondary vortices increase with an increase in t/c for the same α . The strength of the vortices shed increases with t/c , which subsequently results in stronger vortex interactions in the wake. This results in an increased movement of the front stagnation point and the deflections of the wake, as can be seen by comparing the streamfunction plots of Figures 4(a) and 9(a). The rotation of the interacting vortices can also be noted for the $t/c = 0.25$ case. Another point to be noted for this case is the elongation of the vortical structure containing multiple vortices in the wake, due to mutual interaction and their subsequent tearing [see Figure 9(a) at $t = 15.3$ and Figure 10(a) at $t = 13.8$]. The average lift is larger for the $t/c = 0.1$ cases for the same angle of attack, even though the maximum in lift is higher for $t/c = 0.25$. Negative values of lift are obtained for the $t/c = 0.25$ case, which occurs more frequently than for $\alpha = 10^\circ$. This occurrence of negative lift is due to significant movement in the front stagnation point and the formation of alleyways. This negative lift tells us that the larger t/c cases behave more like a bluff body for the same α , compared to $t/c = 0.1$.

6. CONCLUSION

The unsteady flow past elliptic cylinders is studied via the solution of the 2-D Navier-Stokes equation for two Reynolds numbers (3000 and 10 000) at different angles of attack and thickness-to-chord ratios. The resulting flows are quite complex,

but some common features exist which determine the instantaneous flow field. These are:

- (a) different types of bubble formation (single and multiple bubbles) and their movement over the body;
- (b) the movement of the front stagnation point and the related swinging of the wake;
- (c) the formation of the *alleyway* and the movement of the rear stagnation point depending on the released vortices in the neighborhood of the trailing edge;
- (d) the different strength and the releasing frequency of vortices in the wake—this being a function of the angle of attack and the type of bubble formation.

If the angle of attack is large, then the released vortices are strong and hence remain coherent over larger distance in the wake. During their movement in the wake the vortices interact with each other and form clusters. The stronger the vortices, the more is the tendency to form rotating pairs and triplets. In contrast, the weak vortices show multiple vortex interaction and stronger diffusion.

Compared to conventional aerofoils with sharp trailing edges, here the unsteadiness in the value of lift and pitching moment and the rapid flow acceleration on the lower surface near the trailing edge is due to the rounded trailing edge of an ellipse irrespective of angle of attack, while the change in drag is a function of the angle of attack; for the lower angles of attack, the drag does not vary significantly.

REFERENCES

- ABDALLAH, S. 1987 Numerical solution for the Poisson equation with Neumann boundary condition using non-staggered grid; Part I. *Journal of Computational Physics* **70**, 182–192.
- AMES, W. F., 1992 *Numerical Methods for Partial Differential Equations*. London: Academic Press.
- BRAZA, M., CHASSAING, P. & HA MINH, H. 1986 Numerical study and physical analysis of the pressure and velocity fields in the near wake of a circular cylinder. *Journal of Fluid Mechanics* **165**, 79–130.
- DENG, G. B., GUILMINEAU, E., PIQUET, J., QUEUTEY, P. & VISIONNEAU, M. 1994 Computation of unsteady laminar viscous flow past an aerofoil using the CPI method. *International Journal of Numerical Methods in Fluids* **19**, 765–794.
- KAWAMURA, T., TAKAMI, H. & KUWAHARA, K. 1985 New higher order upwind scheme for incompressible Navier-Stokes equations. *Fluid Dynamic Research* **1**, 145–162.
- KRISHNAMURTHY, M. 1992 An experimental study of two dimensional flow past an elliptic cylinder of axis ratio 1.5 in the critical Reynolds number range. *Technical Report PD EA 9210*, National Aerospace Laboratory, Bangalore, India.
- LEONARD, B. P. 1978 A stable and accurate convective modelling procedure based on quadratic upstream interpolation. *Computational Methods in Applied Mechanics* **19**, 59–98.
- LESIEUR, M. & MÉTAIS, O. 1996 New trends in Large-Eddy Simulations of turbulence. In *Annual Review of Fluid Mechanics* (eds J. Lumley, M. van Dyke, & H. Reed), Vol. **28**. 45–82. Palo Alto: Annual Reviews Inc.
- LUGT, H. J. & HAUSSLING, H. J. 1974 Laminar flow past an abruptly accelerated elliptic cylinder at 45° incidence. *Journal of Fluid Mechanics* **65**, 711–734.
- MEHTA, U. B. & LAVAN, Z. 1975 Starting vortex, separation bubbles and stall: a numerical study of laminar unsteady flow around an aerofoil. *Journal of Fluid Mechanics* **67**, 227–256.
- MODI, V. J. & DIKSHIT, A. K. 1975 Near wakes of elliptic cylinder in subcritical flow. *AIAA Journal* **13**, 490–497.
- MORIKAWA, K. & GRONIG, H. 1995 Formation and structure of vortex systems around a translating and oscillating aerofoil. *Zeitschrift Flugwissenschaften und Weltraumforschung* **19**, 391–396.
- NAIR, M. T. & SENGUPTA, T. K. Dec. 1995 Flow around elliptic cylinders at moderate Reynolds numbers. In *Advances in Mechanical Engineering* (ed. T. S. Mruthyunjaya), Vol. II, pp. 1483–1500, Indian Institute of Science, Bangalore. New Delhi: Narosa Publishing House.

- NAIR, M. T. & SENGUPTA, T. K. 1996 Onset of asymmetry: flow past circular and elliptic cylinders. *International Journal of Numerical Methods in Fluids* **23**, 2765–2780.
- NAJJAR, F. M. & VANKA, S. P. 1995 Simulation of the unsteady separated flow past a normal flat plate. *International Journal of Numerical Methods in Fluids* **21**, 525–547.
- OHMI, K., COUTANCEAU, M., LOC, T. P. & DULIEU, A. 1990 Vortex formation around an oscillating and translating airfoil at large incidences. *Journal of Fluid Mechanics* **211**, 37–60.
- OHMI, K., COUTANCEAU, M., LOC, T. P. & DULIEU, A. 1991 Further experiments on vortex formation around an oscillating and translating airfoil at large incidences. *Journal of Fluid Mechanics* **225**, 607–630.
- OTA, T., NISHIYAMA, H. & TAOKA, Y. 1975 Flow around an elliptic cylinder in the critical Reynolds number regime. *ASME Journal of Fluids Engineering* **109**, 149–155.
- PERRY, A. E., CHONG, M. S. & LIM, T. T. 1982 The vortex shedding process behind two-dimensional bluff bodies. *Journal of Fluid Mechanics* **116**, 77.
- RAI, M. M. & MOIN, P. 1991 Direct simulation of turbulent flow using finite difference schemes. *Journal of Computational Physics* **96**, 15–53.
- SCHNEIDER, G. E. & ZEDAN, M. 1981 A modified strongly implicit procedure for the numerical solution of field problems. *Numerical Heat Transfer* **4**, 1–19.
- SCHUMANN, U. 1987 Direct and large eddy simulation of turbulence. Lecture Series: Introduction to the modelling of turbulence 1987–06, von Karman Institute for Fluid Dynamics.
- SENGUPTA, T. K. & SENGUPTA, R. Sept. 1992 Dynamics of near wake of circular cylinder at high Reynolds numbers. In *Bluff Body Wakes, Dynamics and Instabilities* (eds H. Eckelmann, J. Graham, P. Huerre & P. Monkewitz pp. 89–92, IUTAM symposium, Göttingen, Germany. Berlin: Springer-Verlag.
- SENGUPTA, T. K. & SENGUPTA, R. 1994 Flow past an impulsively started circular cylinder at high Reynolds number. *Computational Mechanics* **14**, 298–310.
- SHINTANI, K., UMEMURA, A. & TAKANO, A. 1983 Simulation of 2D external viscous flows by means of a domain decomposition method using an influence matrix technique. *Journal of Fluid Mechanics* **136**, 277–289.
- WILLIAMSON, C. H. K. 1996 Vortex dynamics in the cylinder wake. In *Annual Review of Fluid Mechanics* (eds J. L. Lumley, M. van Dyke & H. L. Reed), Vol. 28, pp. 477–539. Palo Alto: Annual Reviews Inc.